FLOW IN COMPRESSORS

Passive Vortex Generators as End-Wall Flow Control Elements

Fatma Ceyhun Sahin

Turbomachinery and Propulsion Department, von Karman Institute for Fluid Dynamics, Belgium, sahinc@vki.ac.be

Supervisor: Jean-François Brouckaert

Associate Professor, Turbomachinery and Propulsion Department, von Karman Institute for Fluid Dynamics, Belgium, brouckaert@vki.ac.be

University Supervisor: Tony Arts

Professor, IMMC, EPL, UCL, Belgium, arts@vki.ac.be

Abstract

Low profile vortex generators (VGs), selected with the aid of preliminary numerical simulations, are included into a compressor cascade and their effects are observed in terms of exit plane total pressure and velocity distributions. The orientation of VGs can be optimized according to their possibility of decreasing the global loss or improving the exit angle. Several VG configurations are presented in this study.

Keywords: vortex generator, 5-hole probe, compressor cascade measurements

1. Introduction

The present contribution focuses on losses through a compressor cascade. Preliminary numerical simulations of the investigated blade profile showed that the secondary flows dominate the passage and decrease the performance of compressor dramatically [1]. Independent simulations of the flow around low profile VGs [2] guided the selection of geometrical and location parameters for a VG which is supposed to provide a minimum increase in the boundary layer thickness, and hence the associated loss.
Compressor blades and low profile VGs are combined in the C1 facility. The cascade performance is investigated in terms of total pressure, flow velocity and exit angle. The orientation of a VG in a passage is defined according to the results of a numerical investigation [2] and selected sizes of VGs, considering two different wetted area cases, are tested. VGs are promising when they are at a correct location. According to the numerical simulations, the pressure loss behind the VGs increases with increasing wetted area and also incidence angle [2]. That unavoidable increase in loss is expected and it is not considered in selecting the VGs to be tested.
Even though the initial numerical simulation for low profile VGs were not considering neither the blades, nor the adverse pressure gradient in the flow, the experimental validation shows that they were still useful in selecting a correct incidence angle, since the simulations were evaluated in a comparison base.
Considering the application of VGs in a real turbomachinery passage will not allow symmetry as long as the VGs are implemented inside the passage. Different VGs are also tested at the inlet section of the cascade.

2. Experiments

Behind compressor cascade, 5-hole probe measurements are conducted, half a blade chord downstream of the trailing edge. That is in Fig. 1. Knowing that the flow is symmetricaly in the facility, a plane extending from the cascade end-wall up to half a span length distance from the end-wall is scanned. The inlet stagnation condition is set at 45 mm H_2O relative pressure and the exit of the cascade is at atmospheric pressure. The calibration procedure and the resulting calibration maps for the 5-hole probe were presented in [2].
5-hole probe measurements provide both total pressure and flow direction information. Hence, loss in stagnation pressure as well as the velocity field in the

measurement plane are easily obtained but velocity gradients can only be obtained in pitch-wise and span-wise directions. If vorticity is calculated in order to obtain more information on the flow field, the result is only in the axial direction, $(\frac{\partial v}{\partial z} - \frac{\partial w}{\partial y})\hat{i}$. That value neglects the main flow but includes only secondary flow information. In order to observe the flow separation from the cascade end-walls and from the blade surface, 3-D velocity field information is required. For that purpose, measurements are extended to +/- 5% of the chord length on either side of the principal measurement plane, which is also depicted in Fig. 1. The resulting vorticity is a 3-D vector field,

$$(\frac{\partial v}{\partial z} - \frac{\partial w}{\partial y})\hat{i} + (\frac{\partial u}{\partial z} - \frac{\partial w}{\partial x})\hat{j} + (\frac{\partial u}{\partial y} - \frac{\partial w}{\partial x})\hat{k} \quad (1)$$

where the $\hat{j}$ component is pitch-wise vorticity which will give the information on the axis-span plane and the $\hat{k}$ component will give information on the blade to blade plane since it is the span-wise vorticity.

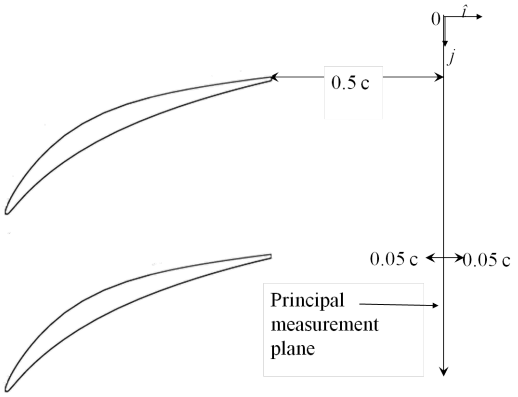

Figure 1: One passage of the cascade and the measurement plane behind it.

3. Configuration of VGs

Low profile VGs altering in terms of geometrical shape are tested. Triangular VGs, having two different sizes, are installed inside the passage and rectangular VGs are installed upstream of the blade leading edge.

3.1. Inside the Passage

A preliminary pressure measurement behind the cascade, installing the triangular VGs at a distance of 1/3 chord behind the leading edge [3] resulted in an increase of the global loss and the flow visualisations in the same study showed that flow separation on the corner was not as early as expected but it was closer to the trailing edge. Hence, for that new study which is focusing on increasing the number of configurations tested, in order to optimize the VG geometry and their positioning, a position which is supposed to have a more positive effect on the corner separation is preferred. Inside the passage, the leading edge of the triangular VG is fixed at a distance of 2/3 chord from the blade leading edge. The distance of a triangular VG from the blade suction surface is always equal to the height of the VG. The orientation of the VG is defined with respect to the inlet flow angle. The positioning of a triangular VG inside the passage is detailed in Fig. 2.

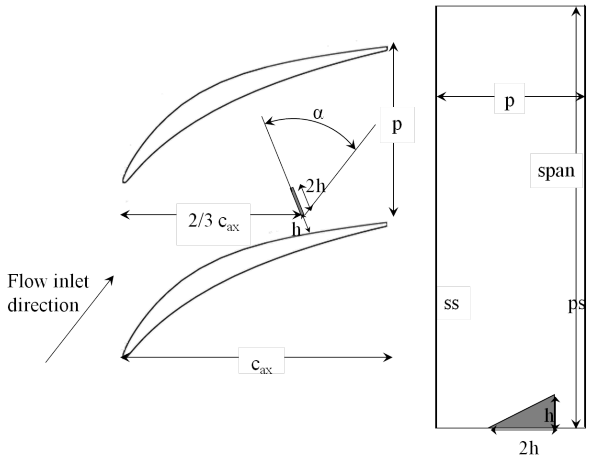

Figure 2: Triangular VG configuration inside the passage.

3.2. Upstream of the Leading Edge

Rectangular VGs are always tested at the inlet section of the passage, 11% of the chord upstream of the leading edge. The angle between the inlet flow and the VG is fixed at 20^o and the position of the VG is changed in the pitch-wise direction. That distance is also referred to the blade leading edge and non-dimensionalised with the pitch length.The rectangular VG configuration at the passage inlet is in Fig. 3.

3.3. Types of VGs

Two different sizes of triangular VGs, h=5 mm and h=10 mm are tested at different incidence angles. Each configuration is named with respect to the VG height as well as the incidence angle. Triangular VGs will be referred as 't', followed with the VG height, h and 'a' will stand for 'angle' followed by the angle

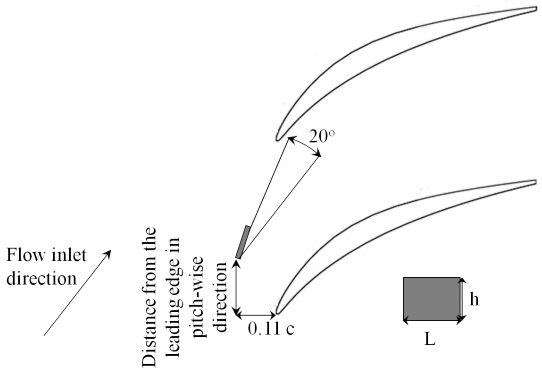

Figure 3: Rectangular VG configuration before the leading edge.

value. For instance, t5a30 will refer to a triangular VG having a height of 5 mm and oriented at 30^o with respect to the cascade inlet flow.
Rectangular VGs, which are referred with an 'r', have a fixed length, L, defined as 10% of the chord. Two different heights, 6.5 mm and 8 mm are tested. 6.5 mm corresponds to 1/3 of the fully developed upstream end-wall boundary layer thickness of the facility and 8 mm corresponds to 1/10 of the blade chord length. The distance of an rVG in the pitch-wise direction from an axial line tangent to the blade leading edge ranges between 0 and 20% of the pitch-length. Hence, an rVG is named like r*hpd* which means r6p10 is a rectangular VG having height of 6.5 mm, at a distance of 10% of the pitch from the leading edge.

4. Measurements

4.1. Stagnation Pressure

The exit stagnation pressure, P_{o_2}, is measured by means of the kiel head of the five hole probe and the corresponding calibration map is used for the incidence correction, which is necessary especially at high angles.

4.2. Total Pressure Losses Behind the Cascade

The chamber pressure, which is the inlet stagnation pressure of the cascade (P_{o_1}), is set at 45 mm H_2O above atmospheric pressure and any possible variation in that level because of the blockage at the exit by the 5-hole probe is checked before each measurement. The stagnation pressure loss behind the cascade is defined as

$$(P_{o_1} - P_{o_2})/(P_{o_1} - p_1) \tag{2}$$

The inlet static pressure, p_1 is calculated according to the calibration of the wind tunnel [3].
The loss value of Eq. 2 is also mass averaged through pitch in order to observe the global effects of the VGs on the flow and also compare those effects at different span-wise positions.

4.3. Flow Angles

The tubes of the 5-hole probe are meant to measure the flow angle within two perpendicular planes. Mass averaging of the angles is also considered to deliver a more robust comparison between different control cases.

4.4. Velocity Field Behind the Cascade

The output of the 5-hole probe, interpreted with four calibration maps, allows obtaining the three components of the velocity in the measurement planes. Subtracting the mean value defined across one pitch allows defining the velocity vectors related to the secondary flow phenomena.

4.5. Vorticity Vectors

The mathematical curl of the velocity vector field, as defined in Eq. 2, defines the vorticity vector field and the components of that vector field are interpreted separately.

4.6. Shape Factor

The characteristics of the boundary layer, developing on the cascade end-wall are obtained considering the axial and span-wise components of the velocity vectors. The shape factor is defined as the ratio of displacement thickness and the momentum thickness [4] where displacement thickness is a discrete integral in that case,

$$\delta^* = \int_0^\delta (1 - u/U)\, dy. \tag{3}$$

As well as the momentum thickness

$$\theta = \int_0^\delta (u/U)(1 - u/U)\, dy. \tag{4}$$

Hence, the shape factor is

$$H = \delta^*/\theta \tag{5}$$

5. Experimental Results

5.1. Base Flow

5.1.1. Total Pressure Losses Behind the Cascade

The base flow total pressure loss as defined in Eq. 2 is depicted in Fig. 4 in terms of a colour map as well as a span-wise distribution of mass average through one pitch. The loss coefficients of the span-wise distribution are non-dimensionalized by the value obtained at mid-span. In the vicinity of the cascade wall, the loss is about 75% of the mid-span loss and it drops to its minimum level, which is almost the half of the loss at the mid-span, about 18 mm away the wall and then the loss starts increasing because of a probable separation from the blade suction side.

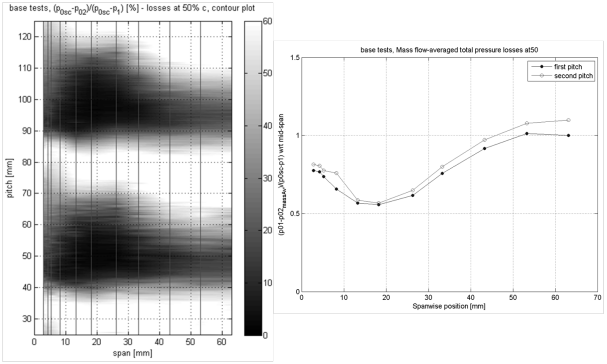

Figure 4: Total pressure loss behind the cascade in case of base flow.

5.1.2. Flow Angles

Mass averaged total pressure loss for base flow case is depicted in Fig. 5 with the averaged pitch angle distribution in order to observe any relation between pressure loss and pitch angle. The pitch angle is also normalized (in terms of a difference) with respect to the value at the mid-span. At the span-wise position where the loss is minimum, the pitch angle has its maximum value and the angle distributions converge approaching to the mid-span. End-wall effects on that angle distribution are dropping the pitch-angle in the vicinity of the end-wall. It is acceptable to consider a passage vortex effect which diverts the flow to the suction side of the neighbouring blade according to that lower angle region observed in Fig. 5.

5.1.3. Velocity Field Behind the Cascade

The secondary velocity vector field for the base flow case is shown in Fig. 6. The blade trailing edge is located at ∼ 81 mm in the pitch-wise direction as

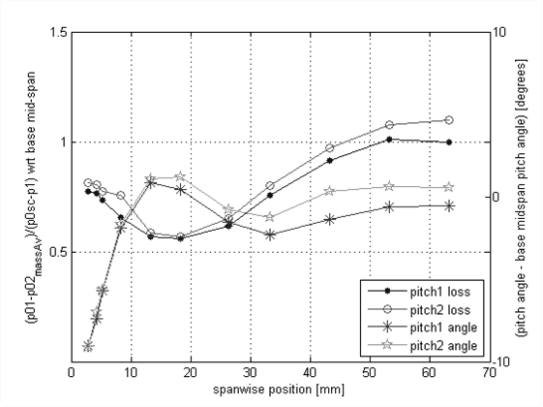

Figure 5: Span-wise distribution of averaged pressure loss and pitch angle.

well as 48.8 mm (=pitch) farther (∼ 130 mm). That reference will be considered in interpreting the figures on the controlled (with VGs) cases. Two components

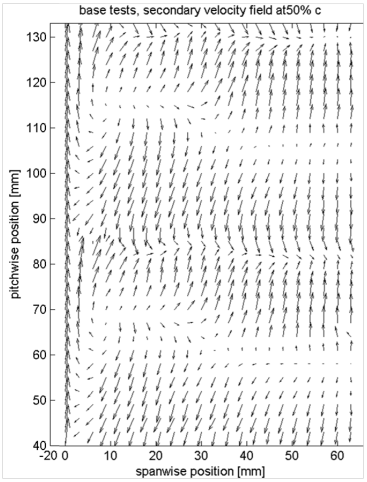

Figure 6: Secondary velocity vector field for base flow.

of the vorticity, from Eq. 1, on the principal plane of measurements are shown in Fig. 7 and Fig. 8, respectively. The position of trailing edge, that corresponds to the maximum loss on that plane, is indicated in those figures as horizontal lines. Fig. 7 includes also the shape factor of the boundary layer developing on the cascade end-wall. The highly viscous region close to the end-wall is easily observed in Fig. 7. The shape factor indicates an unstable boundary layer behaviour besides a probable separation in the wake. In Fig. 8, vortices are observed in couples where the positive signed ones are at a pitch-wise position corresponding to the pressure side of the blade and the negative

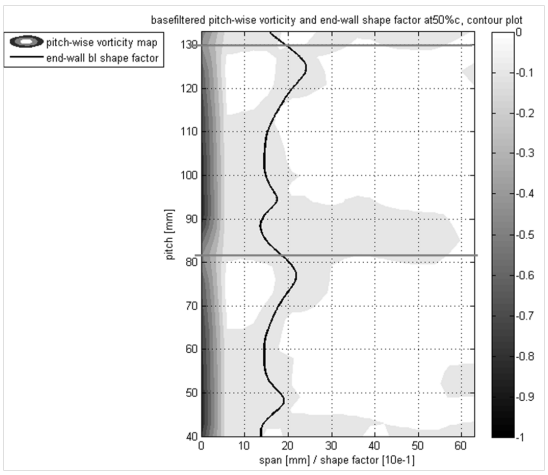

Figure 7: Pitch-wise vorticity map and end-wall shape factor for the base flow.

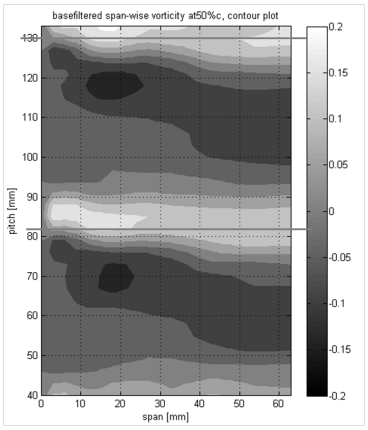

Figure 8: Span-wise vorticity map for the base flow.

signed ones are on the suction surface and they extend up to counter-rotating component of the adjacent vortex closer to the mid-span which also corresponds to the high loss region for the stagnation pressure.

5.2. Controlled Flow

5.2.1. Triangular VGs

Triangular VGs are implemented in the facility according to the configuration defined in Fig. 2.
The triangular VG with a height of 5 mm, VG5, is tested at three different incidence angles with respect to the inlet flow of the cascade. Total pressure loss distributions are shown in Fig. 9 respectively for VGs incidence angle of 20^o, 30^o and 53^o with respect to the cascade inlet flow angle. Those figures are not easy to be distinguished from each other. In the following figure, Fig. 10, the averages over one pitch, normalized with the loss coefficient of the base flow at mid-span, are compared with the base flow case and the effect of VGs are easier to be observed. The integral of the losses are also on the figure. A very clear observation before calculating the integral is that the VG incidence angle 20^o case is the only case which is promising to provide a loss reduction. After varying

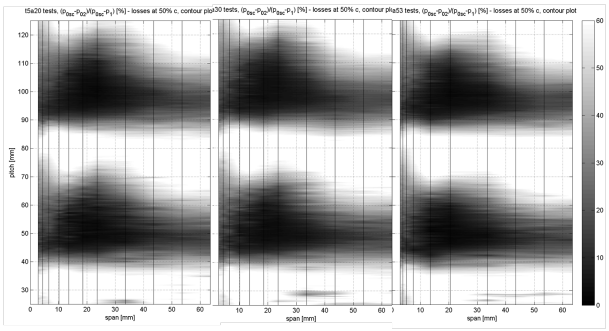

Figure 9: Total pressure loss maps behind the cascade controlled with VG5.

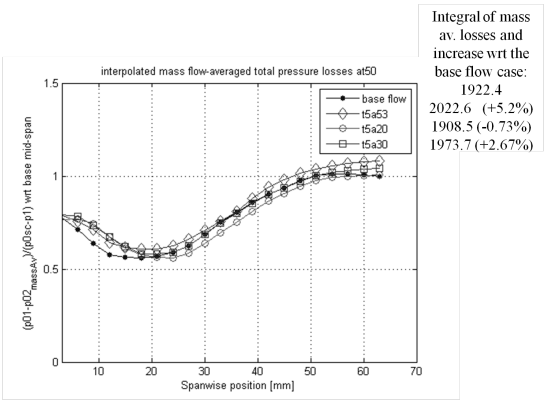

Figure 10: Mass flow rate averaged pressure loss behind cascade with VG5.

the VG incidence angle, the VG height is also varied and in Fig. 11 pressure loss maps for VG incidence angles of 20^o and 53^o, respectively, are depicted. Since VG10 has a wetted area four times larger than the one of the previous case, different effects of it according to the incidence angle are observed on those maps. When the VG incidence angle is low, the disturbance from VG10 is more quickly suppressed approaching the mid-span. Instead of comparing two VG10 cases with the base flow, they are also compared with VG5 cases at the same VG incidence angle. The integral under the mass averaged curves of Fig. 12 shows that at low incidence angle, it is possible to reduce the to-

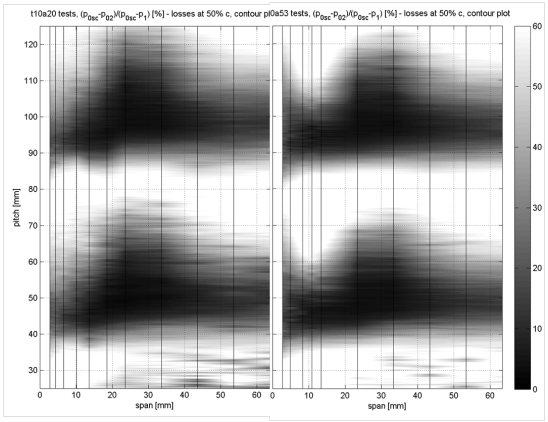

Figure 11: Total pressure loss maps behind the cascade controlled with VG10.

tal pressure loss regardless of the VG height and although larger VG drops it more after 22 mm from the end-wall, local increase behind VG10 results with less global reduction. The comparison of mass averaged losses behind VGs at 53^o, in Fig. 13 shows that global loss increases are unavoidable behind a large VG at large incidence angle. The comparison of the av-

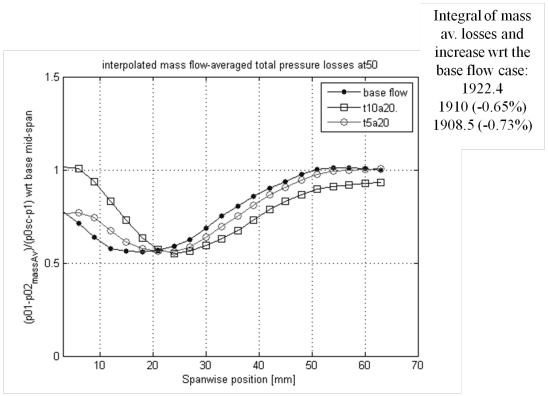

Figure 12: Mass flow rate averaged pressure loss behind cascade with triangular VGs at 20^o.

eraged pitch angles is in Fig. 14. Distributions are once more shown as the difference from the base flow mid-span value. The lower incidence angles of VG5 have no effect on the pitch angle up to a distance of 40 mm from the end-wall and then their effect is increasing the pitch angle slightly. On the other hand, the high VG incidence angle cases decrease the pitch angle constantly up to 30 mm from the end-wall and then its decreasing effect is stronger. The mass average values of pitch angles are compared for a given incidence angle behind different heights of triangular VGs in

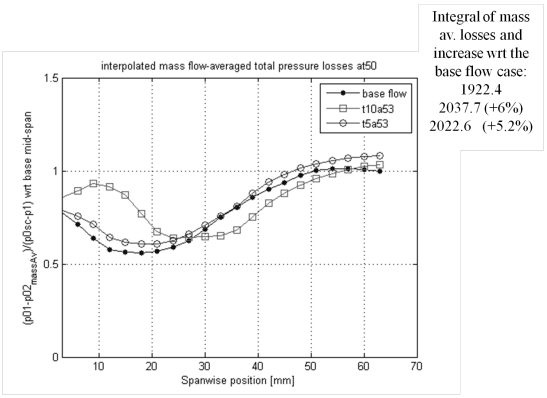

Figure 13: Mass flow rate averaged pressure loss behind cascade with triangular VGs at 53^o.

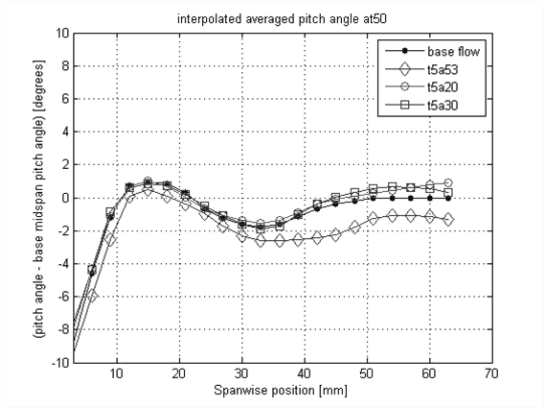

Figure 14: Pitch angle behind cascade with VG5 averaged thorough one pitch.

Fig. 15 and Fig. 16. The lower incidence angle cases are in Fig. 15. The triangular VG10 is useful in avoiding the significant drop in pitch angle in the end-wall vicinity, also recalling that global pressure loss drops behind it. If regions closer to mid-span are considered, VG10 is still more beneficial compared to VG5, considering the effect on the pitch angle. A higher incidence angle for VG10 causes the most significant drop in pitch angle, closer to mid-span, Fig. 16. The pitchwise component of the vorticity vectors, $\frac{\partial u}{\partial z} - \frac{\partial w}{\partial x}$, is depicted in Fig. 17 for VG5 controlled cascade cases, respectively for 20^o, 30^o and 53^o. The shape factor of the cascade end-wall boundary layer is also plotted on top of the vorticity maps. The shape factor value near the blade increases compared to the base flow case and the maximum shape factor location is shifted closer to the suction surface of the blade with low incidence angle. The secondary peak of the shape factor distribution through the pitch is decreased at lower incidence

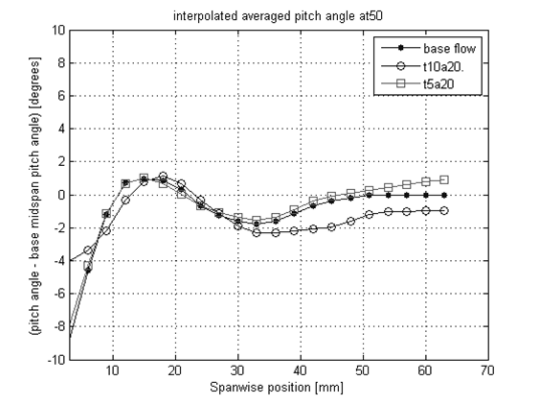

Figure 15: Pitch angle behind cascade with triangular VGs at 20^o averaged thorough one pitch.

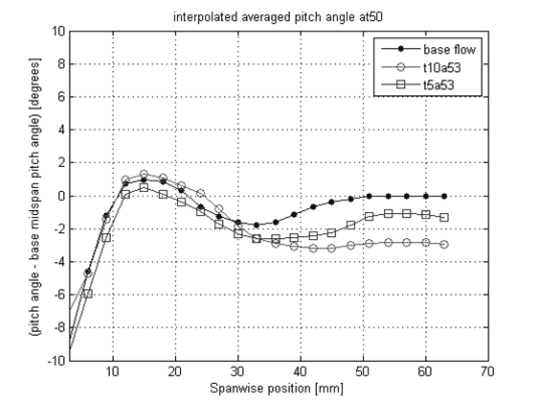

Figure 16: Pitch angle behind cascade with triangular VGs at 53^o averaged thorough one pitch.

angles.

The span-wise vorticity, $\frac{\partial u}{\partial y} - \frac{\partial v}{\partial x}$ component for the VG5 controlled cases are shown in Fig. 18. A couple of stronger counter-rotating vortices are observed in the end-wall vicinity, where the effects of VGs still exist. The pitch-wise and span-wise vorticity distributions for VG10 are depicted in Fig. 19 and Fig. 20, respectively, with the corresponding shape factors. The secondary peak of the end-wall boundary layer shape factor is dropped by VG10 at 20^o significantly and the increase of shape factor behind the blade is less than the one for the VG5 tests. It also worth to recall that t10a20 is able to provide a decrease in both global loss and mid-span pitch angle. Weaker span-wise vortices seen in Fig. 20 compared to Fig. 18 might be a sign of an earlier merge of vortices generated by VG10.

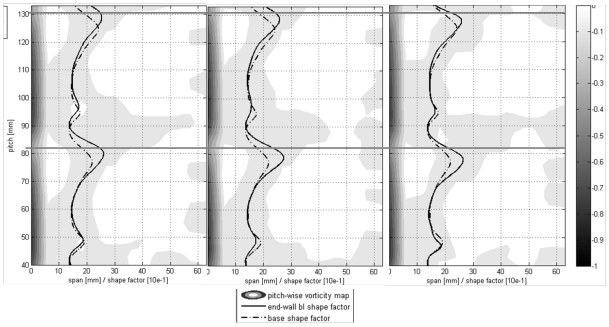

Figure 17: Pitch-wise vorticity map and shape factor for the cascade end-wall behind the cascade controlled with VG5.

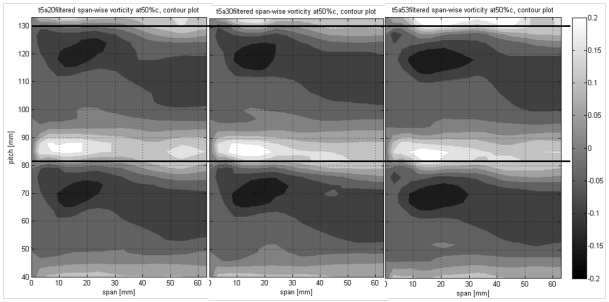

Figure 18: Span-wise vorticity map behind the cascade controlled with VG5.

5.2.2. Rectangular VGs

Since the VGs are implemented on both end-walls, the symmetry of the cascade flow is perfectly kept. However, in real application of VGs inside compressor passages, it is not possible to have VGs larger than the gap between casing and the blade tip. Hence, if the symmetry of the passage needs to be kept, a better position to start controlling the flow should be upstream of the blades. For that configuration, rectangular VGs are suggested. Rectangular VGs are fixed in the upstream section according to Fig. 3. Initially, three different positions through the pitch are tested. Those are, VGs aligned with the leading edge, at a distance of 10% and 20% of the pitch away from the suction side reference of the blade. The distributions of total pressure loss for r6p0, r6p10, r6p20, respectively are shown in Fig. 21. When the VG is aligned with the trailing edge, the generated loss is higher than the one in the other cases. Mass averaged results are compared in Fig. 22. As the distance of 10% pitch length gives the minimum increase of global loss, there must be an optimum pitch-wise position of the rectangular VG on that axial position. Also square VGs are tested at 10% pitch position. The loss distribution is plotted

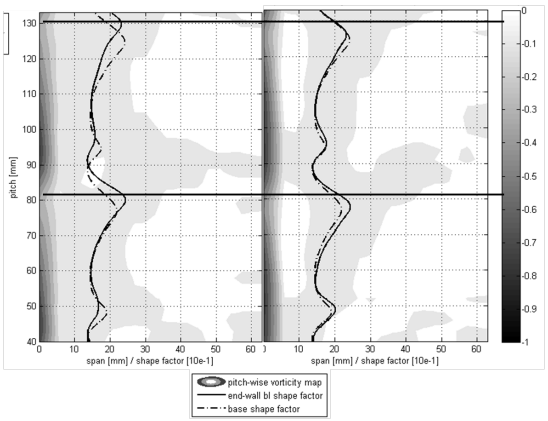

Figure 19: Pitch-wise vorticity map and shape factor for the cascade end-wall behind the cascade controlled with VG10.

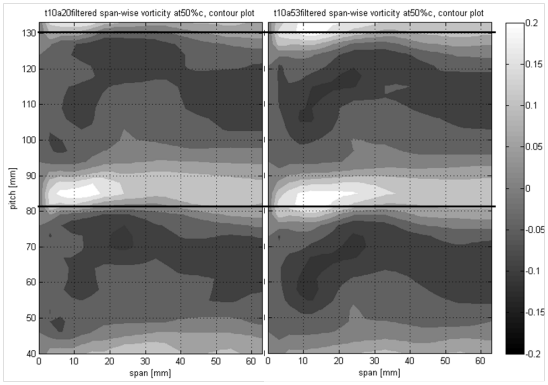

Figure 20: Span-wise vorticity map behind the cascade controlled with VG10.

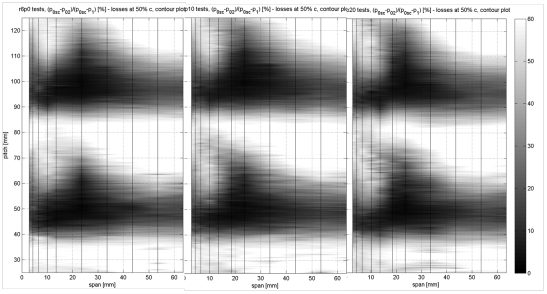

Figure 21: Total pressure loss maps behind the cascade controlled with VG6.

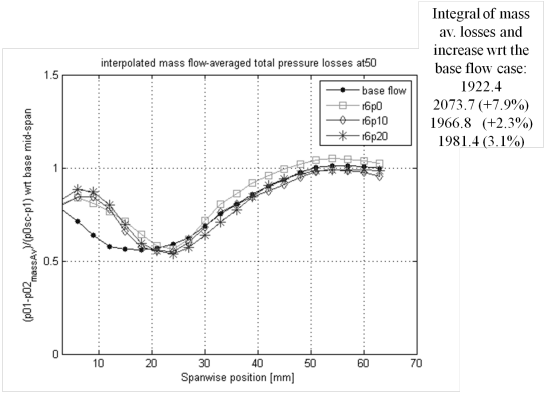

Figure 22: Mass flow rate averaged pressure loss behind cascade with VG6.

in Fig. 23 and compared with r6p10 case in Fig. 24. The repeatability of those measurements have to be satisfied before claiming that VG geometry should be described with respect to the blade geometry rather than flow properties. The effects of the rectangular VG on the pitch angle are compared in Fig. 25. Among the cases presented in Fig. 25, r6p0 is the only one which provides a constant drop of the pitch angle, through span. On the other hand, as VG6 is further to the pressure side of the adjacent blade, it constantly increases the pitch angle distribution and $\sim$ 25% VG height difference have an insignificant effect on the pitch angle despite the unexpected effect on the mass averaged loss distribution. The effect of rectangular VGs in pitch-wise and span-wise vorticity are shown in Fig. 26 and Fig. 27, respectively. The distance of 10% of the pitch from the suction surface is candidate to be an optimum position in dropping the local end-wall boundary layer shape factor as well as for global mass averaged loss. Since the generation of vortices are much earlier than that by VGs located inside the passage, span-wise vortices are weaker in the measurement plane, compared to the previous plots. The results behind the cascade controlled with square VG8 are shown in Fig. 28 and Fig. 29. An expected result of increasing the VG height is observed in Fig. 28 such that the decreasing effect of r6p10 on the shape factor disappears.

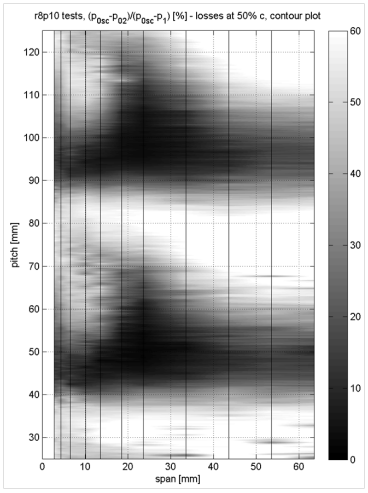

Figure 23: Total pressure loss map behind the cascade controlled with VG8.

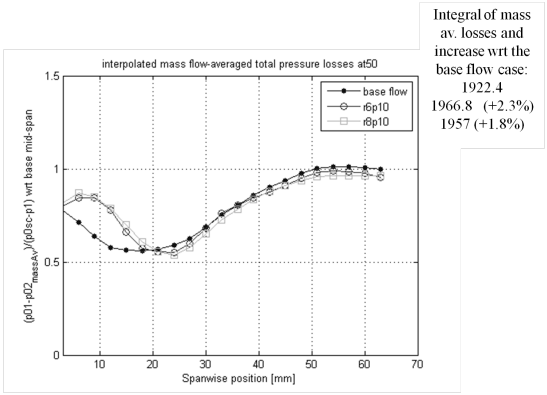

Figure 24: Mass flow rate averaged pressure loss behind cascade with rVGs at 10% of the pitch.

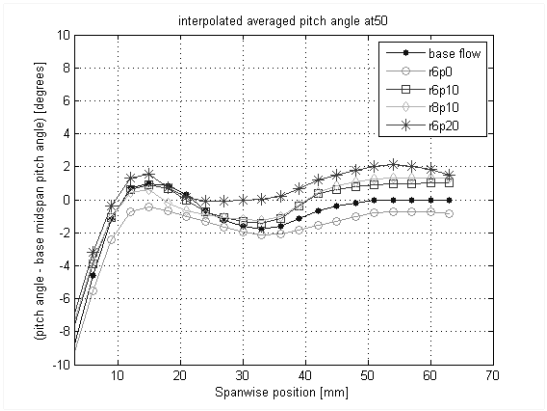

Figure 25: Pitch angle behind cascade with rVG averaged thorough one pitch.

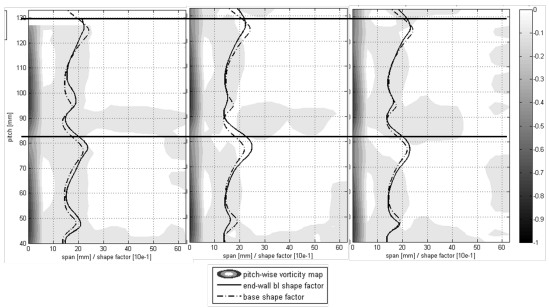

Figure 26: Pitch-wise vorticity map and shape factor for the cascade end-wall behind the cascade controlled with VG6.

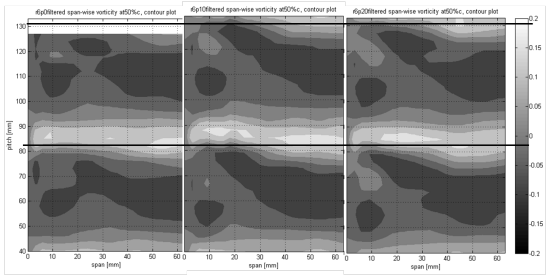

Figure 27: Span-wise vorticity map behind the cascade controlled with VG6.

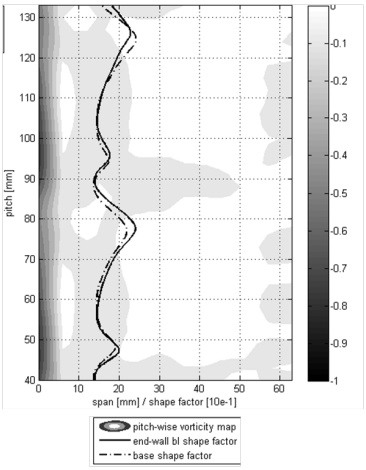

Figure 28: Pitch-wise vorticity map and shape factor for the cascade end-wall behind the cascade controlled with VG8.

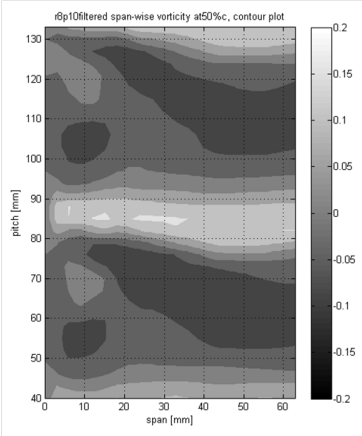

Figure 29: Span-wise vorticity map behind the cascade controlled with VG8.

6. Conclusion

If the design parameter is only the global loss behind the cascade, triangular VGs inside the passage, at a relatively low incidence angle are useful in dropping the loss in total pressure although they cause local increase in the level behind themselves.
Another important parameter should be related to the end-wall boundary layer. If the shape factor from the cascade end-wall is considered, rectangular VGs before the blade leading edge are able to provide a local decrease of end-wall shape factor, where increase of that value behind the blades is unavoidable in any case. VG10 at 20^o gives the minimum local end-wall boundary layer shape factor. Another case which provides such a local drop in end-wall shape factor is the rectangular VG6 at a distance of 10% of the pitch length from the blade suction surface.
The effect of VGs on mass averaged pitch angle is contradictory with their effect on the mass averaged total pressure loss, except t10a20 case.
Considering the three parameters, total pressure loss, shape factor and pitch angle, among the tested control cases, triangular VG10 at 20^o is the best candidate to be focused on as a secondary flow control device.

7. Future Plans

In order to figure out optimum pitch-wise position for rVG6, 15% of the pitch length will be tested as a control location.
The trend of pressure loss is decreasing as the incidence angle of tVG is decreased. However, instead of a continuous decrease with the incidence angle, an optimum angle is expected. Hence, lower incidence angle between the inlet flow and the VG cases will be tested.
Although the repeatability of base flow is verified after each controlled case measurement, none of the controlled cases are ensured in that term. The tests for randomly selected cases will be repeated on the main measurement plane at certain span-wise positions.

References

[1] Sahin, F.C., Boundary Layer Separation Control on a Compressor Blade, in: Summaries of VKI's Doctoral Candidate Research 2009-2010, Sint-Genesius Rode, Belgium, 2010.
[2] Sahin, F.C., Design of a Compressor Cascade for Flow Control Tests, in: Summaries of VKI's Doctoral Candidate Research 2010-2011, Sint-Genesius Rode, Belgium, 2011.
[3] Albiero, A., Aerodynamic Performance of End-Wall Flows, SR 2011-05, von Karman Institute for Fluid Dynamics (May 2011).
[4] Kiock, R., Boundary Layers on Turbomachinery Blades, CN 118, von Karman Institute for Fluid Dynamics (1983).

The Effect of Solidity on Compressor Performance and Stability

Jérôme Sans

Turbomachinery and Propulsion Department, von Karman Institute for Fluid Dynamics, Belgium, sans@vki.ac.be

Supervisor: Jean-François Brouckaert

Associate Professor, Turbomachinery and Propulsion Department, von Karman Institute for Fluid Dynamics, Belgium, brouckaert@vki.ac.be

Co-Supervisor: Tony Arts

Professor, von Karman Institute of Fluid Dynamics, Turbomachinery and Propulsion Department, Belgium, arts@vki.ac.be

University Supervisor: Philippe Chatelain

Professor, Université Catholique de Louvain, Institute of Mechanics, Materials and Civil Engineering, Belgium, philippe.chatelain@uclouvain.be

Abstract

The solidity in a compressor is the ratio of the aerodynamic chord over the pitch. The following PhD project aims at investigating numerically and experimentally the effect of the solidity on both compressor performance and stability. A low-pressure compressor stage designed and manufactured by TechSpace Aero and representative of a state-of-the-art booster helps to support the study. Existing compressor correlations are reviewed to extract the influence of solidity on deviation, incidence and losses. The issue of the optimum solidity is also covered. Then, the effect of solidity is assessed by CFD thanks to FINE/Turbo of NUMECA International. Rotor and stator blade numbers of TechSpace Aero's booster are varied independently to generate different compressor stages. The performance of all the configurations are assessed from choke to stall. The effect of solidity on pressure ratio, efficiency and stall limit is discussed.

Keywords: Compressor, solidity, pitch, chord, blade number

Nomenclature

Roman symbols

c	[m]	Aerodynamic chord length
s	[m]	Pitch
t	[m]	Blade thickness
M	[-]	Mach number
p	[Pa]	Pressure
V	[m/s]	Absolute velocity
W	[m/s]	Relative velocity
Z	[-]	Blade number
D	[-]	Diffusion factor
D_{eq}	[-]	Equivalent diffusion ratio
C_p	[-]	Static pressure coefficient

Greek symbols

β	[°]	Flow angle
γ	[°]	Stagger angle
δ	[°]	Deviation angle
ϕ	[°]	Camber angle
θ	[m]	Momentum thickness
σ	[-]	solidity
ρ	[kg/m^3]	Density
ω	[-]	Total pressure losses
Ψ_a	[-]	Zweifel coefficient

Acronyms

DCA	Double circular arc
LP	Low pressure
MCA	Multiple circular arc
VKI	von Karman Institute

Subscript

0	Stagnation condition
1	Upstream condition
2	Downstream condition
s	Static condition
i	Ideal condition
θ	Tangential direction

1. Introduction

The solidity is the ratio of the aerodynamic chord over the peripheral distance between two blades also called the pitch. This parameter must be selected early in the design process and the important role played by the solidity in the loading assessment makes its choice a crucial step that should be regarded with great care. Despite some spurious attempts to define an optimum solidity in terms of loading or efficiency, no general rule exists to guide the designer in this choice.

In the last decades, a constant increase of solidity in engine compressors has been noticed (Fig. 1). This reflects the need for the engineer to satisfy more and more severe high loading requirements that can only be achieved with high solidity. As shown in Fig. 2, the solidity trend observed over the last 50 years is mainly explained by the use of long-chord blades (i.e. low aspect ratio[1]) which brought many experimental evidences of stability enhancements and a better behaviour with respect to secondary flows [2] (A. J. Wennerstrom, 1989). However, this chord enlargement is limited by the axial extent of the compressor which is imposed by mechanical requirements. Some improvements might still emerge by looking at the pitch effect that is directly linked to the blade number.

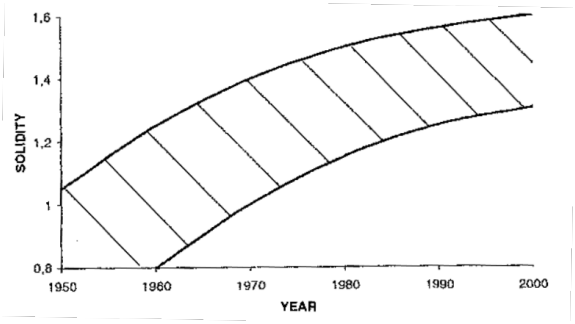

Figure 1: Evolution of the solidity in engine compressors over the last years [1] (T. Obrecht, 2006).

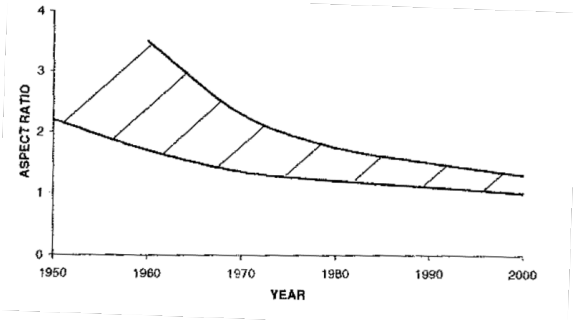

Figure 2: Evolution of the aspect ratio in engine compressors over the last years (T. Obrecht, 2006).

Unfortunately, even though either a chord extension or a blade number increase allows to work at higher loading, both methods present the undeniable disadvantage of increasing the engine weight, meaning a higher fuel consumption and pollutant emissions. It is therefore essential to fully understand the benefits and the drawbacks when adjusting those parameters. In that prospect, the following PhD project aims at investigating numerically and experimentally the effect of the solidity on both compressor performance and stability. As a support to this investigation, the low-pressure compressor stage studied at VKI within the framework of the DREAM project is considered. The stage has been designed and manufactured by TechSpace Aero and is representative of a state-of-the-art booster. Its performance has been assessed both numerically with the CFD software FINE/Turbo^{TM} from Numeca International and experimentally in the VKI R4 facility.

The first part of the work covers all the existing

[1]The aspect ratio is defined as the ratio of the blade height over the aerodyamic chord.

compressor cascade correlations and tries to characterize the influence of solidity on deviation, incidence and losses. The role played by solidity on the blade loading is addressed and existing optimum solidity criteria are presented.

After reviewing the literature, the effect of solidity is assessed through CFD. The study is achieved in 3D using the complete geometry and design conditions of the baseline booster of the DREAM project. Different stage configurations are analyzed by changing the blade number of both rotor and stator. The focus is set on the impact on pressure and efficiency as well as the stability margin.

2. Literature review

Two main issues are addressed in this section. Firstly, correlations from cascade tests are reviewed. Despite the fact that the flow in axial compressors is mainly governed by three-dimensional effects, cascade theory allows to shed some light on the physical phenomena taking place in the three-dimensional machine. These correlations essentially come from the 1960's and may have been corrected since then by engine manufacturers. However, all compressor designers once dealt with those data. Secondly, the question of the optimum solidity is studied.

2.1. Cascade correlations

The geometrical definitions given in Fig. 3 are the NASA-SP36 conventions used in the rest of the document ([3], 1965). The angles are referred to the axial direction and usually given in degrees.

- β_1 relative inlet flow angle;
- β_2 relative outlet flow angle;
- κ_1 inlet blade metal angle;
- κ_2 outlet blade metal angle;
- ϕ camber angle;
- i incidence angle;
- δ deviation angle;
- γ stagger angle;
- c aerodynamic chord;
- s pitch.

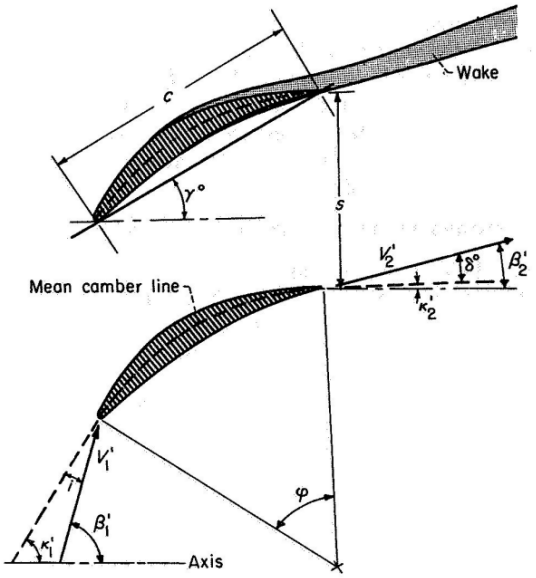

Figure 3: Geometrical configuration and angle definition in a compressor cascade

The three parameters commonly used to characterize the performance of compressor cascades are the incidence, the deviation and the pressure losses. The angles are defined in Fig. 3 while the losses are given by Eq. 1.

$$\bar{\omega} = \frac{p_{02} - p_{01}}{p_{01} - p_{s1}} \tag{1}$$

The minimum loss incidence is considered as the reference incidence and is illustrated in Fig. 4. For NACA65 and DCA blades, cascade performance has been studied at low Mach number ($M < 0.3$) and for various solidities as well as different thicknesses, camber angles and inlet flow angles[2].

Knowing the type of blade (NACA65 or DCA), the turning to be achieved, the maximum thickness and the solidity, the designer is able to calculate the minimum loss incidence and deviation. For an arbitrary blade and design requirement (for example, a DCA blade and design angle of $\beta_1 = 50°$) and applying NASA's correlation, Fig. 5 and Fig. 6 show that varying the camber or the maximum thickness to chord ratio, deviation always decreases with solidity.

This highlights the guidance role of the solidity in cascade: the higher the solidity, the better the flow

[2] All the results are available in the NASA design book [3] but are not copied here for the sake of clarity.

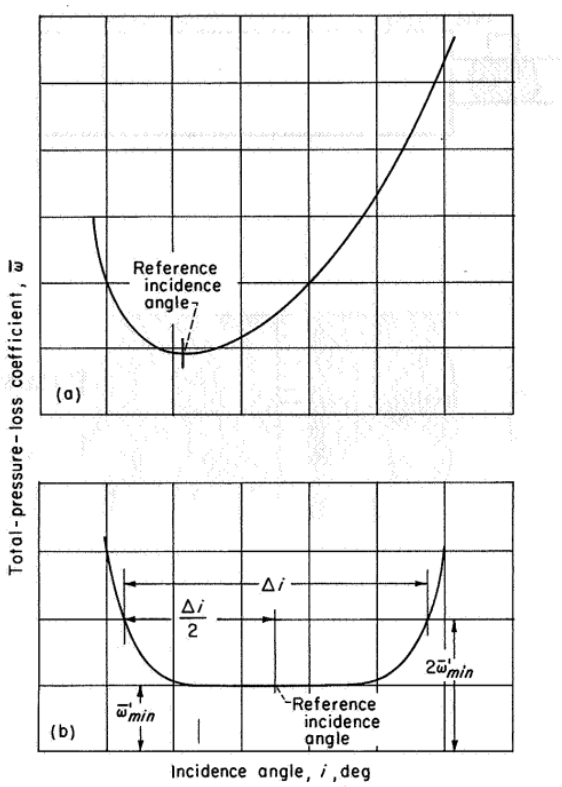

Figure 4: Definition of the reference incidence angle:(a) minimum loss angle clearly defined; (b) minimum loss angle taken as the mean of the incidence angle range defined by the angles where the losses reach twice its minimum value.

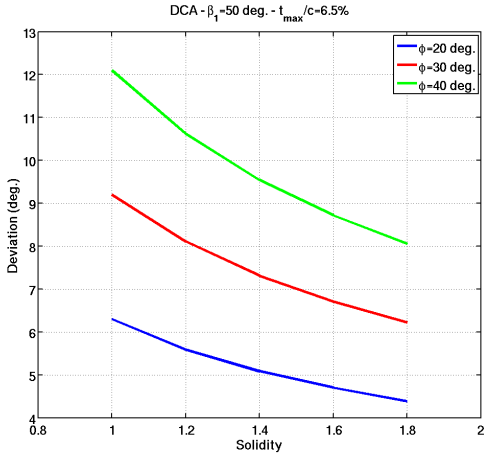

Figure 5: Deviation at minimum loss incidence following NASA SP36 correlations for a DCA blade: $\beta_1 = 50°$ constant maximum thickness to chord ratio of 6.5% and varying camber angle.

follows the blade and the lower is the deviation. This had already been pointed out by Carter ([4], 1949).

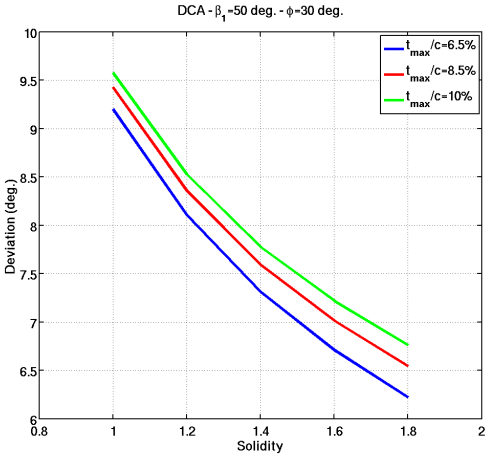

Figure 6: Deviation at minimum loss incidence following NASA SP36 correlations for a DCA blade: $\beta_1 = 50°$ constant camber angle of 30° and varying maximum thickness to chord ratio.

Indeed, the famous Carter's rule, given by Eq. 2, relates the deviation to the camber and the solidity, and allows to establish the same conclusion.

$$\delta = m\phi\sqrt{\frac{1}{\sigma}} \tag{2}$$

The empirical coefficient m of Eq. 2 has been tabulated by Carter [4]. In practise, Carter's rule is still used but, nowadays, NASA's correlation are considered as more reliable, more accurate and more systematic.

The solidity also plays an important role in the blade loading. The loading assessment is essential to characterize in which conditions the blade is operating and how far it is from stall.

The first attempt in characterizing the loading comes from Zweifel in 1945 [5]. He compared the lift of the blade to a reference lift based on the outlet velocity. After arrangement, the Zweifel coefficient Ψ_a is given below:

$$\Psi_a = \frac{\Delta V_\theta (V_1 + V_2)}{\sigma V_2^2} \tag{3}$$

To establish this coefficient, Zweifel relied on different cascade tests from turbines and compressors. Surprisingly, this coefficient has the remarkable property that for many different blades the minimum drag-lift ratio is independent on the inlet and outlet

air angles β_1 and β_2 and always lies between $\Psi_a = 0.9$ and $\Psi_a = 1$. This is illustrated in Fig. 7.

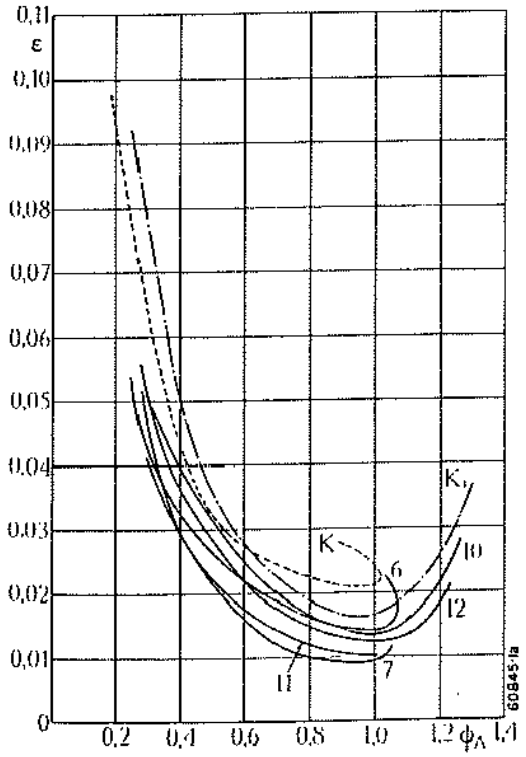

Figure 7: Drag-lift ratio in function the Zweifel loading factor Ψ_a for different type of blading [5] (O. Zweifel, 1945).

This makes it possible to define an optimum pitch distance to operate at maximum lift-drag ratio for given β_1 and β_2. Hence, given upstream and downstream flow angles and velocities, the optimum pitch distance required for maximum lift-drag ratio (i.e. $\Psi_a = 0.9$) can be determined. The data used by Zweifel mainly come from turbine cascade tests but his method can be trusted to select an optimum pitch -at least as a first guess- in compressor blade design. Eck ([6], 1973), Wallis ([7], 1983) or Dixon ([8], 1998) refer to Zweifel's optimum pitch distance when designing optimum fan blades. This parameter is also mentioned by T. Obrecht in [1] to address the loading of compressor blades.

Regarding the assessment of the loading and the stability limit of cascades, the greatest advancement comes from Lieblein and his diffusion factor in 1953 [9]. It was admitted that the suction side boundary layer, facing an adverse pressure gradient, was responsible for the limiting pressure rise and turning of the flow. Therefore, Lieblein linked the suction side deceleration of the flow to a local diffusion factor:

$$D_{loc} = \frac{V_{max} - V_2}{V_2} \tag{4}$$

where V_{max} is the peak suction side velocity and V_2 the outlet velocity. Under the form of Eq. 4, the calculation of the diffusion factor was very time-consuming and not practical. A simplified diffusion factor was then defined to assess the loading of the blades:

$$D = (1 - \frac{V_2}{V_1}) + \frac{\Delta V_\theta}{2V_1\sigma} \tag{5}$$

This simplification brings up the outlet-inlet velocity ratio, the tangential velocity difference as well as the solidity. Then, Lieblein put the wake momentum thickness in relation with the diffusion factor for many various types of blading as illustrated in Fig. 8 from [3]. The wake momentum thickness starts

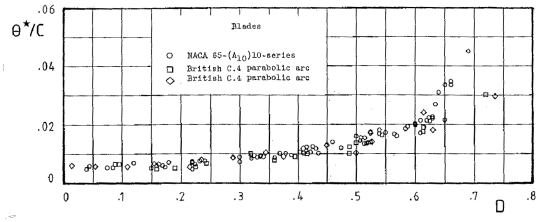

Figure 8: Variation of the wake momentum thickness with diffusion factor [3] (W. H. Robbins, R. J. Jackson, S. Lieblein, 1965).

to rise more steeply for diffusion factors above 0.6. Therefore, a diffusion factor of 0.6 has been selected as the inception of blade stall.

However, because the measurement of the blade momentum thickness is not always realizable, Lieblein proposed to use loss parameters which would mainly rely on the total pressure losses and flow angles and which would closely approach the wake momentum thickness. Those are given by:

$$\frac{\theta}{c} \approx \frac{\omega \cos(\beta_2)}{2\sigma} \tag{6}$$

$$\frac{\theta}{c} \approx \frac{\omega \cos(\beta_2)}{2\sigma} \left(\frac{\cos(\beta_2)}{\cos(\beta_1)}\right)^2 \tag{7}$$

All Lieblein's results are gathered on Fig. 9 using the loss parameters of Eq. 6 and Eq. 7. Plotted in function of the diffusion factor, the two curves of Fig. 9 offer good approximations of Fig. 8.

The loss parameter of Eq. 6 is the most common one (because it is easier to measure) and the most widely quoted in the literature. It remains more or less constant and close to 0.007 until a diffusion level of 0.6 is reached. However, the second loss parameter of Eq. 7 looks to be a better indicator of stall.

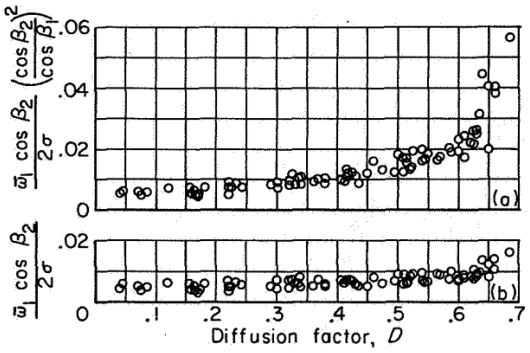

Figure 9: Variation of downstream losses in function of the diffusion factor [3] (W. H. Robbins, R. J. Jackson, S. Lieblein, 1965).

The work of Lieblein allows to shed light on the role played by the solidity in the appraisal of the loading and the losses. An increase of solidity allows to reduce the diffusion factor but gives more total pressure losses. It also helps to lower the diffusion ratio and, then, to delay the stall emergence. When the solidity decreases, the losses follow. However, if the diffusion ratio approaches its limit, high diffusion losses appear and the flow may separate completely. The designer is thus confronted to a trade-off between low losses (choosing low solidity) and high stability (choosing high solidity).

Later, Lieblein provided new correlations of momentum thickness (and loss parameter) in terms of an equivalent diffusion ratio [10]. This equivalent diffusion ratio expresses the ratio of the maximum suction side velocity to the inlet velocity. This approach encountered a great support and has been used and adapted by many as Koch and Smith ([11], 1976) or Wright and Miller ([12], 1991). It is widely accepted that Koch's data are the most complete and accurate. However, in the prospect of this paper, Lieblein's data are more convenient to understand the role played by the solidity in the loading assessment and the loss development.

The influence of the Mach number must also be mentioned. Heilmann et al. ([13], 1968) showed that the effect of solidity is not independent of Mach number. It seems that going to slightly supersonic Mach numbers, it is better to keep the solidity as high as possible to avoid important shock losses.

2.2. The optimum solidity

It has been shown in the previous section that higher solidities go with higher losses while lower solidities induce higher diffusion and then higher losses. Somewhere in between those two extreme situations sits an optimum solidity. As presented on Fig. 7, research from Zweifel already exposed an optimum loading sitting between $\Psi_a = 0.9$ and $\Psi_a = 1.0$. For given inlet and outlet velocity triangles, this suggests that an optimum solidity can be selected using Eq. 8.

$$\sigma_{\text{opt}} = \frac{\Delta V_\theta (V_1 + V_2)}{\Psi_{a_{\text{opt}}} V_2^2} \tag{8}$$

where $\Psi_{a_{\text{opt}}}$ must be chosen between $\Psi_a = 0.9$ and $\Psi_a = 1.0$. The same manipulation could be done with Lieblein's diffusion factor but no criterion which defines an optimum diffusion factor exist.

Another method had already been offered by Howell in the 1940's ([14]). He observed that the nominal tangential deflection was only depending on the solidity and he found out that the best solidity could be calculated using Eq. 9.

$$\tan(\beta_1) - \tan(\beta_2) = \frac{1.55}{1 + \dfrac{1.5}{\sigma}} \tag{9}$$

Even though Howell's work is considered as a reference and was used for a long time, nowadays, it is considered not to be reliable anymore.

More recently, in 1988, A. B. McKenzie published an quite appealing method to get the optimum solidity ([15]). According to his results the solidity which leads to the best efficiency is linked to an ideal static pressure rise given by:

$$C_{p_i} = \frac{p_{s_2} - p_{s_1}}{1/2\, \rho_1 w_1^2} = 1 - \frac{\rho_2}{\rho_1} \left(\frac{w_2}{w_1} \right)^2 \tag{10}$$

As plotted in Fig. 10, the optimum pitch-chord ratio (in terms of maximum efficiency) appears to be a linear function of the ideal static pressure rise Eq. 11.

$$s/c = 9(0.567 - C_{p_i}) \tag{11}$$

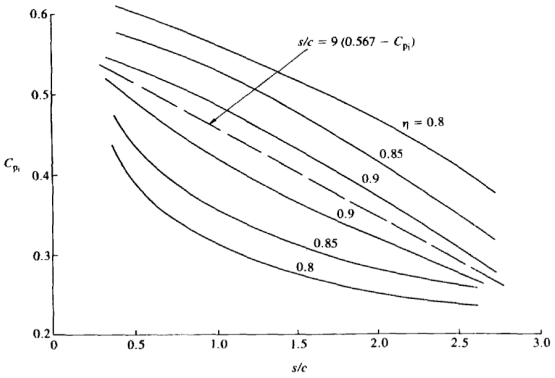

Figure 10: Efficiency contours in function of pitch-chord ratio s/c and ideal static pressure rise C_{p_i} [15] (A. B. McKenzie, 1988).

Considering the case of the DREAM project booster and its rotor inlet and outlet conditions available in Table 1, the different methods have been compared to each other and to the actual solidity of the booster. The results are presented in Table 2. Only Zweifel's method gives realistic solidities.

	Span location	β_1	β_2	w_1	w_2
Velocity	Hub	49°	18°	263 m/s	207 m/s
Triangle	Mid	48°	28°	255 m/s	197 m/s
Data	Tip	49°	38°	252 m/s	192 m/s

Table 1: Rotor inlet and outlet velocity triangles of the DREAM project booster

Optimum solidities					
	Span location	Howell	Zweifel $\Psi_a = 0.9$	McKenzie	State-of-the-art
σ	Hub	1.76	1.63	0.54	1.52
	Mid	0.90	1.25	0.61	1.28
	Tip	0.49	0.98	0.59	1.26

Table 2: Solidity recommendations from Howell's, Zweifel's, and McKenzie's methods

The issue of the optimum solidity can also be approached by considering the loss correlation: for given inlet and outlet velocity triangles there exists only one solidity that produces the minimum amount of losses. Indeed, knowing the upstream and downstream velocity triangles the diffusion factor is only a function of the solidity. Hence, whatever loss parameter is used, the total pressure losses also become a function of one single variable being the solidity. Finally, the solidity which gives the minimum loss is the solution of the minimization problem summarized below:

$$\left.\begin{matrix}\beta_1\\ \beta_2\\ V_1\\ V_2\end{matrix}\right\} \rightarrow D = g(\sigma) \rightarrow \omega = f(\sigma)$$

Then,

$$\sigma_{opt} =: \left\{\sigma \text{ such as } \frac{d\omega}{d\sigma} = 0\right\}$$

The method has been applied using Lieblein's correlations of Fig. 9(b). Hearsey ([16], 1986) gives a reliable polynomial fit of this correlation given by Eq. 12.

$$\frac{\omega \cos(\beta_2)}{2\sigma} = 0.004 + 0.004722\, D + 0.095679\, D^3 \quad (12)$$

Using the mid-span velocity triangle data of Table 1, Fig. 11 presents the losses as a function of the solidity. Lines of constant diffusion factor are also available in Fig. 11. The minimum loss solidity sits around 0.8. This corresponds to a diffusion factor higher than 0.45. This method could be applied with more accurate loss correlation as Koch and Smith provided in [11]. However, as no constraint is set on the loading it will always result in very low solidities which have high diffusion and offer very poor stability margins.

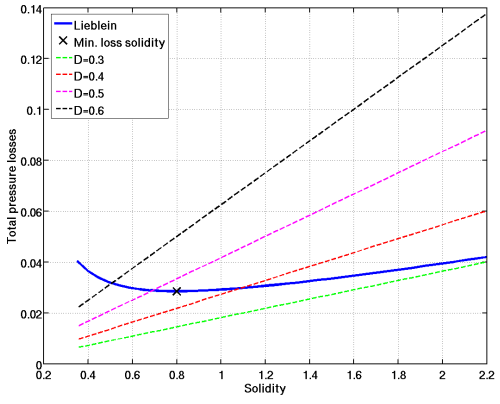

Figure 11: Evolution of losses in function of solidity using correlation of Fig. 9(b) and mid-span data of Table 1.

3. Numerical investigation

Two investigations have been performed. The first one studies the effect of rotor blade number while the second looks at the influence of stator blade number. Both are based on the DREAM project booster. This LP compressor is a 1.5 stage composed of inlet guide vanes, a rotor and a stator. The compressor has been studied at VKI both numerically with the commercial software FINE/Turbo of NUMECA International and experimentally in the high-speed R4 facility[3]. A 3D view of the 1.5 stage is available in Fig. 12.

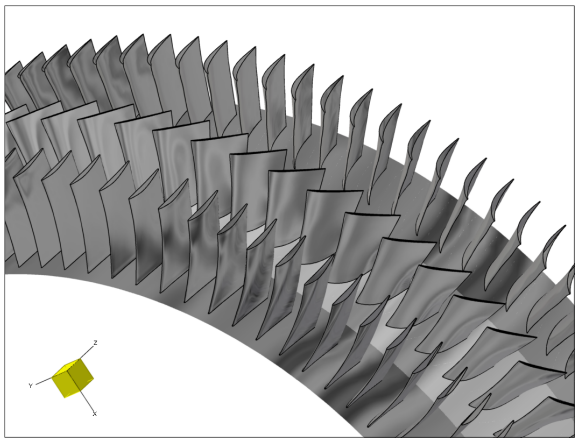

Figure 12: Three-dimensional view of the 1.5 stage (inlet guide vanes, rotor, stator).

3.1. Set-up

The whole 1.5 stage is considered but the rotor and stator blade numbers are varied independently. For each different blade number a new mesh has been created. The mesh of baseline and its properties are extensively described in [17]. In order to optimize the post-processing the number of points and configuration of the meshes remain constant and only the blade periodicity is varied from one case to another.

The boundary conditions are part of the specifications of TechSpace Aero as well as the turbulence model that is the low Re Yang Shih k-ϵ model. The compressors have been throttled by increasing the static pressure at stator outlet and always ensuring the radial equilibrium. Approaching the stall region the back-pressure has been raised iteratively to find the last stable conditions. This point has been considered as the stall point.

The booster has been designed in a way that the stall starts from the rotor hub (between 20% and 40% of the blade height from the hub). This may unfortunately compromise the stability analysis of the compressor.

3.2. Influence of rotor blade number

The performance of three different rotors have been assessed from choke to stall. The corresponding blade numbers are indicated in the Table 3. The rotor

Tested rotor solidities				
	Blade number	σ_{hub}	σ_{tip}	Relative to design (%)
Design	66	1.32	1.09	-15%
	76	1.52	1.26	-
	86	1.72	1.43	+15%

Table 3: Tested rotor blade numbers and solidities

pressure ratio and efficiency are plotted in Fig. 13 and Fig. 14. Looking at Fig. 13, it appears that the high

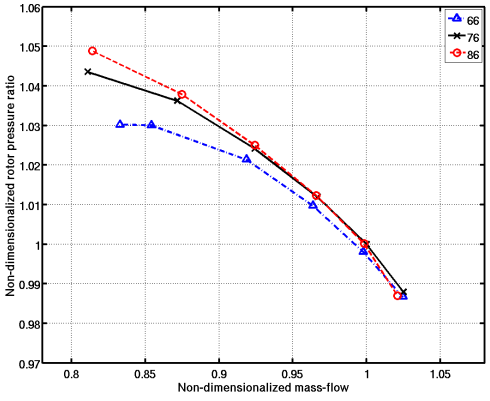

Figure 13: Rotor pressure ratio versus mass-flow for 66, 76 and 86 rotor blades on DREAM compressor.

solidity rotor achieves the highest pressure ratio. This is in agreement with cascade theory or Carter's rule (Eq. 2) which predicts that the deviation is reduced when the solidity increased. As the deviation is lower, the flow turning increases and more pressure rise is achieved. However, the situation is not so obvious at choke.

[3]The experimental results have not been published yet while the whole numerical investigation can be found in [17].

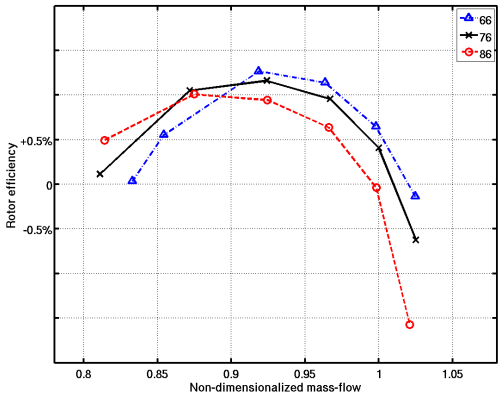

Figure 14: Rotor efficiency versus mass-flow for 66, 76 and 86 rotor blades on DREAM compressor.

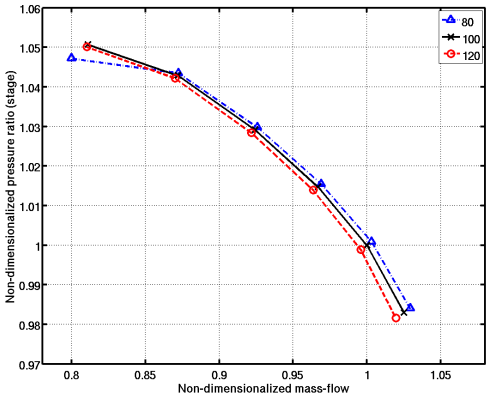

Figure 15: Stage pressure ratio versus mass-flow for 80, 100 and 120 stator blades on DREAM compressor.

The effect on the maximum efficiency is clear and the lowest solidity shows the best efficiency. This is rather expected as cascade correlations predict less losses for low solidity. Nonetheless, the trend does not remain the same on the whole operating range. The low solidity rotor is the less stable. This is most probably coming from a very high diffusion on the blades. No improvement appears between the mid and the high solidity rotors which is quite unexpected and requires a deeper analysis.

3.3. Influence of stator blade number

The influence of stator solidity has also been studied by changing the number of vanes. The tested stator solidities are available in the Table 4. In terms

Tested stator solidities				
	Blade number	σ_{hub}	σ_{tip}	Relative to design (%)
Design	80	1.47	1.46	-20%
	100	1.83	1.82	-
	120	2.20	2.19	+20%

Table 4: Tested stator blade numbers and solidities

of efficiency and pressure ratio, the effect of stator solidity is more straighforward than for the rotor. Removing blades improve both pressure ratio (Fig. 15) and efficiency (Fig. 16). When there is no work addition, a blade row only represents a source of friction losses that decrease the total pressure. Then, the same temperature rise is achieved whatever the number of blades while less pressure losses are encountered when less stator vanes are present. It results in

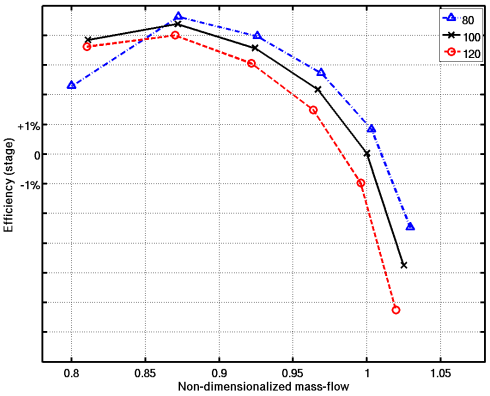

Figure 16: Stage efficiency versus mass-flow for for 80, 100 and 120 stator blades on DREAM compressor.

a higher pressure ratio and a higher efficiency. The opposite happens when adding some blades. These conclusions are in agreement with cascade correlations. Between the stages with 100 and 120 stator blades no difference appears in terms of stability. The low solidity stator stalls before the others. Although reducing the stator blade number might have transposed the stall inception in the stator, a complete three-dimensional analysis of the flow is required to understand the stall behaviour of the stage.

4. Conclusion

The solidity effect has been reviewed in the literature and some existing optimum solidity criteria have been presented. A numerical investigation

has been performed in order to see some effect on the booster designed and manufactured by Techspace Aero within the framework of the European DREAM project. Both rotor and stator blade numbers have been varied independently to analyze their impact on the compressor performance. It appeared that:

- the higher the solidity, the lower the deviation and the better the guidance;
- the higher the solidity, the higher the losses (and the lower the efficiency).

For a rotor, the better guidance results in a higher turning and consequently, to a higher pressure ratio. A stator only sees a higher solidity as a source of higher losses. This is reflected in both lower efficiency and pressure ratio.

To be complete, this study must be extended to different types of blades and different compressors. A blade generator has already been implemented at VKI in order to generate through CFD a more extensive database than the one of the 1960's NASA correlations. This blade generator is able to create NACA65 (A10-series), DCA, MCA or wedge profiles. They all have their own range of application and definitely have different behaviours regarding solidity variations. For each type of blade, incidence, turning, inlet Mach number and solidity must be varied. A cascade configuration will be set up and solved in FINE/Turbo. Some examples of the blade generator capabilities are plotted in Fig. 17.

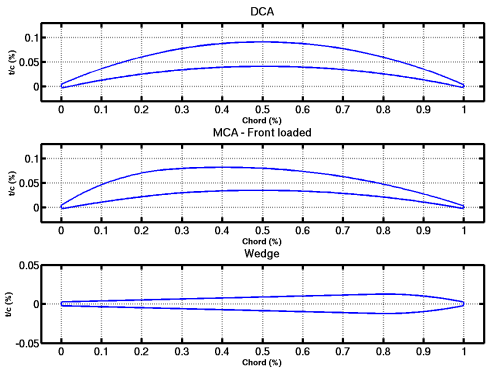

Figure 17: Profiles generated with the VKI blade generator.

Other three-dimensional test cases may be investigated. Until now, only Techspace Aero's booster has been considered. A fan stage which presents slightly supersonic tip regions could highlight the influence of Mach number on the effect of solidity. This could support previous work from Heilmann et al. [13].

The final validation of this study will be cascade tests in the C3 high-speed facility of VKI. This experimental part would focus on the validation of the CFD database.

Acknowledgments

This research is supported by TechSpace Aero.

References

[1] T. Obrecht, HP compressor preliminary design, in: Advances in axial compressor aerodynamics, von Karman Institute for Fluid Dynamics Lecture Series, Belgium, 2006.
[2] A. J. Wennerstrom, Low aspect ratio axial flow compressors: why and what it means, Journal of Turbomachinery 111 (4) (1989) 357–365.
[3] W. H. Robbins, R. J. Jackson, S. Lieblein, Aerodynamic design of axial-flow compressors, NASA SP-36 (1965).
[4] A. D. S. Carter, The low-speed performance of related aerofoils in cascades, A.R.C. Tech. Report, NGTE (September 1949).
[5] O. Zweifel, The spacing of turbo-machine blading, especially with large angular deflection, The Brown Boveri Review.
[6] B. Eck, Fans, Pergamon Press, 1973.
[7] R. Wallis, Axial flow fans and ducts, John Wiley & Sons, Inc., 1983.
[8] S. Dixon, Fluid mechanics, thermodynamics of turbomachinery, 4th Edition, Butterworth-Heinemann, 1998.
[9] S. Lieblein, Diffusion factor for estimating losses and limiting blade loadings in axial-flow compressor blade elements, Tech. rep., NACA, Lewis Flight Propulsion Laboratory, Cleveland, Ohio (June 1953).
[10] S. Lieblein, Loss and stall analysis of compressor cascades, Journal of Basic Engineering 81 (4) (1959) 387–400.
[11] C. C. Koch, L. H. J. Smith, Loss sources and magnitudes of axial flow compressors, Journal for Engineering for Power.
[12] P. I. Wright, D. C. Miller, An improved compressor performance prediction model, in: Proceedings of Institution of Mechanical Engineering, 1991.
[13] W. Heilmann, H. Starken, H. Meyer, Cascade wind tunnel tests on blades designed for transonic and supersonic compressors, Tech. rep., Institut fuer Luftstrahlantriebe, AGARD-CP-34 (1968).
[14] A. R. Howell, Fluid dynamics of axial compressors, in: Proceedings of Institution of Mechanical Engineering, Vol. 153, 1945.
[15] A. B. McKenzie, Fluid dynamics of axial compressors, in: Proceedings of Institution of Mechanical Engineering, Vol. 202, 1988.
[16] R. M. Hearsey, Practical compressor aerodynamic design, in: Adanced topics in turbomachinery technology, 1986.
[17] J. Sans, Numerical investigation of a single stage axial compressor, PR 2010-10, von Karman Institute for Fluid Dynamics (2010).

Accelerated Optimization for Multi-Disciplinary Design of Transonic and Contra-Rotating Turbomachinery Components

Michael Joly

Turbomachinery and Propulsion Department, von Karman Institute for Fluid Dynamics, Belgium, joly@vki.ac.be

Supervisor: Tom Verstraete

Assistant Professor, Turbomachinery and Propulsion Department, von Karman Institute for Fluid Dynamics, Belgium, verstraete@vki.ac.be

Supervisor: Guillermo Paniagua

Associate Professor, Turbomachinery and Propulsion Department, von Karman Institute for Fluid Dynamics, Belgium, panigua@vki.ac.be

University Supervisor: Paul Cizmas

Professor, Aerospace Engineering Department, Texas A&M University, cizmas@tamu.edu

Abstract

Optimization techniques offer promising perspectives for the design of complex turbomachinery components. To limit the weight of current and future aero-engine configurations, the number of stages tends to be reduced and more power output is expected from each blade row. The design of highly-loaded components is subsequently multi-disciplinary, with concurrent objectives in terms of aerodynamic efficiency and structural integrity. To speed up the process of an aero-mechanical optimization, the implementation of Computational Fluid Dynamics (CFD) solvers on Graphics Processing Units (GPU) is investigated in a first part. Turbines operating in the transonic regime experience shock waves. To limit the mechanical stress induced by the vane-rotor shock interaction, it is proposed in a second part to optimize the vane geometry to attenuate its downstream distortion. The impact on the stage will be evaluated by computing the unsteady forcing on the following rotor. In a third part, the design of contra-rotating fans is investigated in order to produce compact and highly-loaded configurations. The proposed methodology enables one to achieve a complete design, from the flow path definition to the aero-mechanical characterization of the fan.

Keywords: Multidisciplinary Optimization, GPU Accelerated CFD, Transonic Turbine, Contra-Rotating Fan

1. Introduction

The design of innovative turbomachinery components for compact high-speed propulsion flight vehicle or for limited fuel burns of current aircrafts requires to reduce the number of stages to save weight. A reduction of the size of the machine leads to an increase of the load on each single components. The related design challenges are inherently multidisciplinary. Trade-offs between aerodynamic efficiency and structural integrity have to be found and optimization strategies provide promising perspectives.

Compared to traditional design strategies, optimization techniques, such as Evolutionary Algorithms, are able to augment the explored design space and to consider simultaneously several conflicting objectives. To speed up the most expensive Computational Fluid Dynamics (CFD) evaluation of an aero-mechanical design problem, parallel computations could be performed, typically using several Central Processing Units (CPU). Alternatively, much work has recently been focused on Graphics Processing Units (GPU) and applications of GPU in aerospace highlighted the potential acceleration of computing time from 10 to 20 times faster [1, 2]. The present project proposes in a first part to investigate GPU-accelerated CFD.

Optimization techniques are then applied to inves-

tigate innovative design methodologies for turbomachinery configurations involving demanding fluid and solid requirements. In particular, high-pressure turbines operate in the transonic regime leading to strong shock interactions between the vane and the rotor blades. To limit the risk of high-cycle fatigue on the rotor, the vane could be designed for limited downstream distortion. A design approach with steady-state evaluations to reduce the shock waves propagation downstream of the vane is proposed. The impact on the stage will be evaluated by computing the unsteady forcing on the following rotor.

The design of transonic fans reveals also strong compromises between aerodynamic and structural considerations. While conventional fans produce a pressure ratio of about 1.6, many research trends focus on much higher loads. A design methodology to achieve highly-loaded fan is investigated in this project. As an alternative to traditional 1-D parametric studies, an optimization of the flow path is performed to initiate the aerodynamic design of the fan. To by-pass any two-dimensional sub-optimal results, a three-dimensional optimization is directly processed, including several section profiles along the span, as well as lean and sweep. High-fidelity CFD and Finite Element structural analysis are employed to guaranty the aerodynamic efficiency and the structural integrity of the finalized design. This methodology will be extended to the design of contra-rotating fans.

2. Implementation of GPU Accelerated CFD for Optimization of Turbomachinery Components

The present project targets the development of a CFD solver with GPU capacities, aiming at the integration of fast and robust Navier-Stokes evaluations into aero-mechanical design-optimization strategies.

2.1. Implementation of a Multi-Block CFD solver

In preparation prior to implementation on GPU, a multi-block viscous solver is implemented on conventional CPU. Both H and O4H mesh topologies are considered (See O4H topology in Figure 1). The class orientation of the C++ language is extensively used to make the code as generic as possible, making an adaptation to other topology very practical. The structured mesh is initialized by an algebraic grid and then smoothed with an elliptic method.

In the present status, an Euler solver has been implemented. The convective fluxes are computed with the Roe flux-difference splitting scheme. A

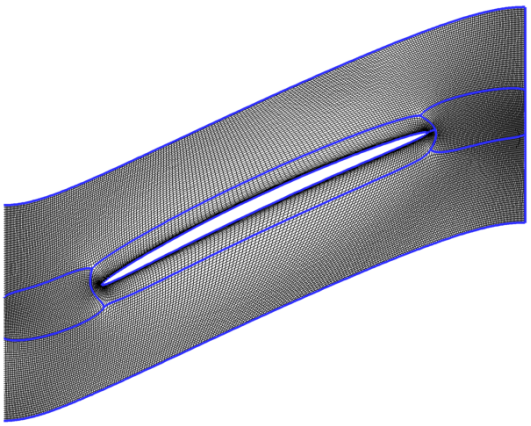

Figure 1: O4H MESH TOPOLOGY

Runge-Kutta time-stepping scheme is employed to obtain a steady-state solution. Boundary conditions of solid wall, inlet and outlet complement the solver. The solver is applied to the geometry of a channel with a bump (bump height = 10% of channel height). Using atmospheric conditions (Pa=101300Pa and Ta=288K), values of total pressure and temperature are fixed at the inlet considering an inlet Mach number. The inlet flow is imposed to be in the axial direction. The back pressure is imposed to be equal to the atmospheric pressure. For the transonic with an inlet Mach number of 0.9, the solution has a shock and is therefore strongly dependent on the grid size. With more refinement, the location of the shock system appears more precisely (See Figure 4). In the present case, the interaction between the shock system and the outlet subsonic boundary leads to some instabilities observed in the convergence history.

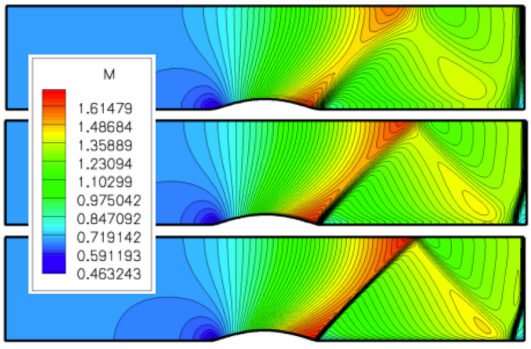

Figure 2: MACH NUMBER FIELD IN A CHANNEL FOR THREE DIFFERENT GRID REFINEMENTS (UP : $130 * 30$, $MIDDLE$: $250 * 60$, $BOTTOM$: $400 * 120$)

2.2. Implementation of CFD solver on GPU

After completion of the multi-block solver, this one would be implemented on Graphics Processing Units (GPUs). A GPU is a processor that exhibits higher level of parallelism than conventional CPUs (higher rate of floating-point operations per second) and has the strong potential to accelerate scientific computing. Extensive parallelism within GPU accelerated CFD requires however significant changes to the implementation of the underlying code. NVIDIA provides in this concern an extension to the C programming language called CUDA [3], in which the developer can set up a large number of threads that are grouped into thread blocks. Each block is then associated with one of the multi-processors of the GPU, where the threads could be scheduled and synchronized to handle memory concerns.

3. Attenuation of Vane-Rotor Shock Interaction in a High-Loaded Transonic Turbine Stage

Turbines operating in the transonic regime experience shock waves. Giles [4] highlighted strong shock interactions between the vane and the rotor. Sieverding et al. [5] described the aerodynamics of the trailing-edge shock system within transonic turbine vanes. On the suction side a left running shock travels downstream in a direct manner towards the rotor (hereafter, direct shock on Figure 3). On the pressure side, a right running shock impinges onto the adjacent vane suction side, generating a hereafter called reflected shock that propagates to the following blade row. Hence, the pressure field in the vane/rotor gap is characterized by two strong static pressure gradients in the pitch-wise direction, related to the passage of direct and reflected shock waves.

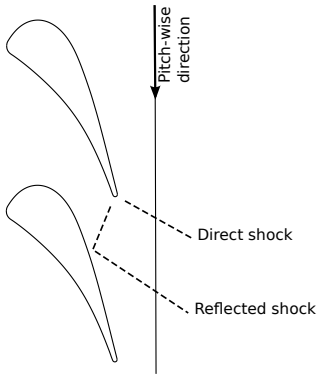

Figure 3: SHOCK SYSTEM DOWNSTREAM OF A TRANSONIC TURBINE VANE

3.1. Objectives

Within the present work, the evolutionary optimization design tool for turbomachinery component, developed at the von Karman Institute [6], is applied to conceive original transonic two-dimensional vanes with limited vane downstream distortion and reduced losses. Aerodynamic performances are evaluated by a steady-flow Navier-Stokes solver.

The distortion downstream of the vane section is assessed by the the standard deviation of the downstream pitch-wise static pressure distribution (eq.1). The region of interest is located 35% of the axial chord, downstream of the stator trailing edge, where the rotor leading edge should be located.

$$\sigma = \sqrt{\int_{y_0}^{y_0+pitch} \frac{(p(1.35 * \lambda, y) - \bar{p})^2}{pitch}.dy} \qquad (1)$$

The second objective is to ensure high efficiency; the kinematic loss coefficient (eq. 2) ought to be minimized [**?**].

$$\xi = 1 - \eta = 1 - \frac{V_2^2}{V_{2is}^2} \qquad (2)$$

3.2. Parametrization and Evaluation

The definition of the parametrization is a crucial step in any optimization problem, since it defines the optimal geometry that can be represented. Each parameter should have a clear impact on the geometry definition, to ease the identification of the optimal set of parameters. Moreover, the design space defined by ranges for each parameter accounts for the available shape variety; if the optimal shape cannot be represented, it will not be found by the optimizer.

Two-dimensional airfoil sections are defined starting from the definition of the camberline by the following set of parameters: axial chord, stagger angle, inlet metal angle and outlet metal angle. The suction and pressure side curve are defined by Bézier curves, for which the control points are specified relative to the camber line. High-pressure turbines are characterized by the passage ducted by two adjacent airfoils and this parametrization enables a detailed control of the throat region (See Figure 4).

The mesh generation is parametrized and can therefore be executed in an automated manner independently of the blade shape. A H-type periodic non-matching mesh is used and particular care is addressed to the meshing of the throat area and the non-matching

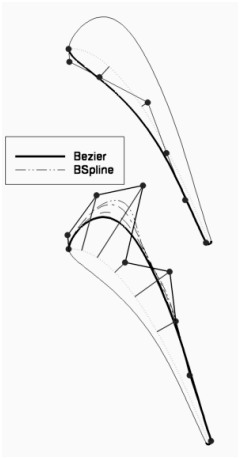

Figure 4: CONTRACTION CHANNEL PARAMETRIZATION

boundaries. The performances of each individual are evaluated with the Navier Stokes sovler TRAF [7]. The Reynolds-Averaged Navier-Stokes equations are solved using a Runge-Kutta time integration and a discretization based on finite volumes with a cell-centered scheme. The two-layer mixing length model of Baldwin and Lomax is used to compute the boundary layer as fully turbulent. The solver shows good agreements with experimental results obtained in the CT3 test facility of the von Karman Institute (See Figure 5).

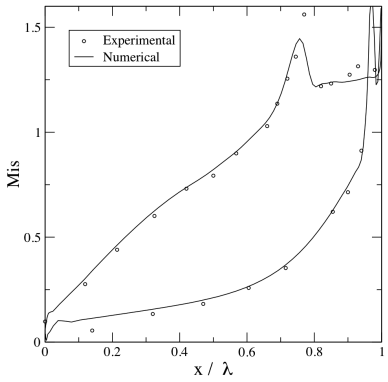

Figure 5: MACH NUMBER DISTRIBUTION ON CT3 VANE

3.3. Optimization

An optimization run with 200 generations of 60 individuals is performed and the evolution of the process is illustrated in Fig. 6. Through the optimization process, the individuals of each population are progressively satisfying the constraints. Hereafter the objective value is minimized. The best candidate obtained with the single-point strategy provides a reduction of 43.2% of the downstream pitchwise static pressure standard deviation. The loss coefficient is 1.4% lower than the baseline, the outlet flow angle 0.02 degree larger and the mass flow increased by 0.3%.

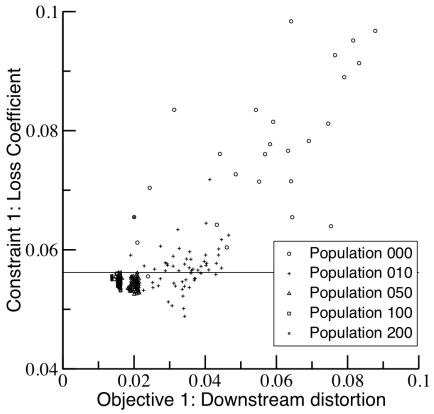

Figure 6: OPTIMIZATION ITERATIONS

On density gradient fields (See Figure 7), the left running shock, i.e. direct shock, clearly appears with lower intensity for the optimized airfoil. By contrast, the right running shock has a stronger intensity than the baseline. Its reflection on the adjacent blade suction side, i.e. reflected shock, appears with higher intensity. A strong impingement on the suction side of the adjacent vane is also observed on the Mach number distribution (See Figure 8, left). With a similar suction side and increased thickness on the pressure side, the contraction channel of the optimized airfoil is narrower than the baseline's. The channels are choked and therefore sonic sections impose the mass flows. For the baseline, the sonic section is located at the end of the convergent channel and coincides with the geometric throat. On the other hand, the channel resulting from the optimized airfoil is convergent-divergent. The sonic section moved upstream and is inclined (See Figure 7). This explains how similar mass flows could be reached with different geometric throats. The convergent-divergent shape of the optimized contraction channel over-accelerates the flow downstream of the sonic line, increasing the Mach number levels on the rear pressure side and mid suction side. With a faster flow within the contraction channel, the trailing edge shock system is modified and the propagation of shock waves downstream is remarkably attenuated (See Figure 8, right).

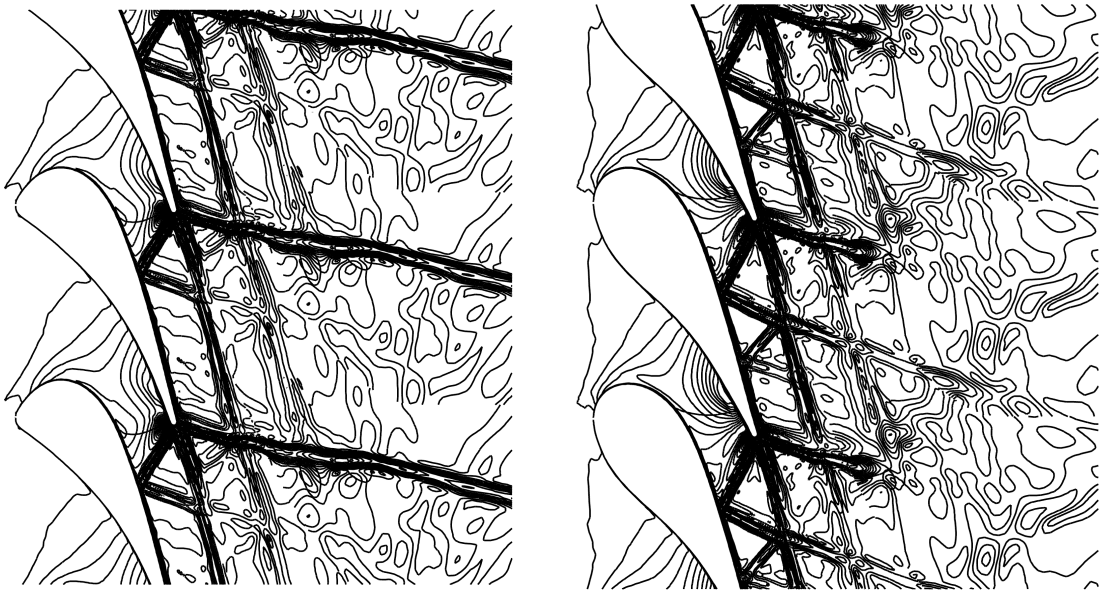

Figure 7: DENSITY GRADIENT FIELDS AND SONIC LINES FOR BASELINE (LEFT) AND OPTIMIZED (RIGHT) GEOMETRIES

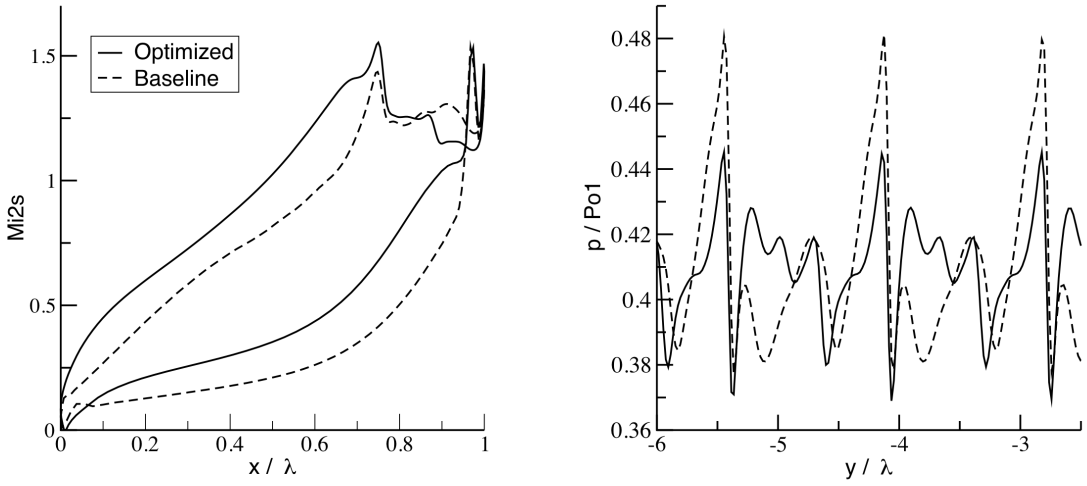

Figure 8: MACH NUMBER ALONG PROFILE AND DOWNSTREAM PITCH-WISE PRESSURE DISTRIBUTIONS

4. Full-Design of Compact Transonic Fan with Optimal Aero-Mechanical Performances

4.1. Design Methodology

The traditional design strategy for transonic fans consists of four successive steps [8]. A preliminary design is achieved with low-fidelity models such as through-flow techniques. Subsequently a blade-to-blade two-dimensional CFD and quasi-three dimensional computations are performed to generate a three-dimensional geometry. Then, a fully three-dimensional viscous optimization is applied to improve the performance considering three-dimensional effects, such as end-bends and secondary losses, introducing sweep and lean to the geometry but without section profiles adaptation. A finite element structural analysis is ultimately performed to assess the geometry.

The main drawback of the traditional fan design strategy is the parametric study employed during the preliminary design phase based on through-flow modeling. Such an approach is not capable of extensively exploring the whole design space. Secondly, the two-dimensional optimization that generates section profiles considers only limited three-dimensional flow patterns, ignoring for example end-walls and secondary flows. The obtained "sub-optimal" profiles then remain constant during the three-dimensional optimization, and the flow angles prescribed by the through-flow model are therefore not optimized during the optimization with the high-fidelity solver. Using this method, through-flow codes, despite being limited in physical modeling, generally fix 80% to 90% of the final fan design.

An improved design methodology is proposed and employs multi-objective optimization at every design steps to achieve the complete aero-mechanical design of a highly loaded axial flow fan. It aims to smooth the intermediate steps between the preliminary design and the three-dimensional aero-structural optimization of the geometry. The through-flow model is first integrated in an optimization loop to enlarge the design space of the preliminary design. It is crucial to consider a wide range of candidates at this early stage of the design, where the end-walls, the blade count, flow angles, and the wheel speed are selected. Through-flow computations, however, do not include any information about blade geometry; only the solidity (i.e. pitch/chord ratio) is considered through correlations. It is then proposed to directly initiate a three-dimensional optimization based on the preliminary design results. Three-dimensional fan rotor geometries are generated from the stacking along the span of chord-wise camber angle and thickness distributions. Possible values of incidence and deviation angles are estimated to define feasible ranges of inlet and outlet metal angles at different radii. The performances of each three-dimensional candidates are assessed simultaneously with fluid and structure evaluations. A viscous flow solver computes the pressure ratio and adiabatic efficiency of the fan, while a finite element solver evaluates its structural integrity.

4.2. Single-Stage Highly Loaded Fan

The methodology is demonstrated for the design a highly loaded axial flow fan. The aim is to produce a compact fan that achieves a similar pressure ratio compared to the NASA rotor 37 (PR=2.1) but with a subsonic inlet relative Mach number at the hub. The expected benefit is an enlarged operating range, allowing the shock system to adapt itself better along the span as the machine is throttled.

A first optimization of the flow path configuration is performed. The through-flow model solves the streamline curvatures and radial gradients at inter-row positions based on the radial equilibrium principle. Losses on the Euler work are introduced based on profile losses and shock losses [9, 10]. The objectives of the through-flow optimization, written in their minimization form, are:

- *1-η*: Maximize the predicted efficiency
- *Tip radius*: Minimize the machine size, considering the end-wall tip radius parameter as a objective
- *for $M_{1ri} > 1.0$, $max(\beta_{2i}-\beta_{1i})$*: Minimize the highest value of relative flow turning over the spans of supercritical profiles, limiting the risk of boundary layer separation at the shock impingement on the adjacent blade suction side

Figure 9 shows Pareto fronts as a result of the through-flow optimization. It can be observed that a higher tip radius allows a higher efficiency and a limited relative flow turning over the span of supercritical profiles. Nonetheless, our interest remains in a reduced radius to achieve maximum compactness. The selected candidate is denoted by a diamond in Figure 9. The configuration obtained is a transonic fan with a subsonic inlet relative Mach number of 0.58 at the hub and a supersonic value of 1.42 at the tip.

The three-dimensional optimization is constrained to produce fan geometries achieving a pressure ratio

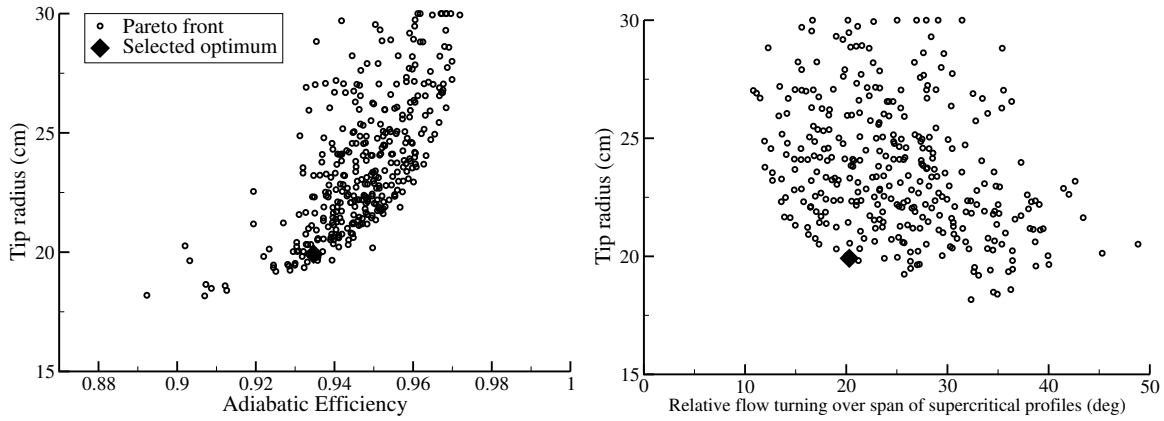

Figure 9: THROUGH-FLOW OPTIMIZATION PARETO FRONT

between 2.1 and 2.2 with a minimum required mass flow rate of 20.2 kg/s at the design point. The objective is to maximize the design-point adiabatic efficiency. The achieved fan geometry provides a pressure ratio of 2.11 with an efficiency of 89% (See Figure 10).

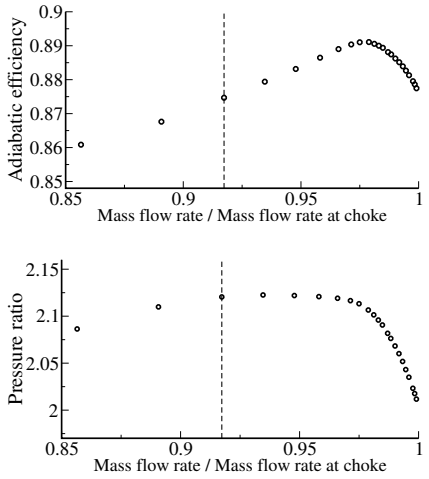

Figure 10: OPTIMAL FAN PERFORMANCES

In transonic fans, a shock system impinges the suction side at higher spans. The high rotational speed of the blade makes the section profiles at high radius reach supersonic speeds. Consequently, a shock originates at the leading edge, with a right-running part hitting the suction side of the adjacent blade and a left-running part propagating upstream (See Figure 11). The flow in the region close to the front suction side is supersonic, and its inclination is therefore influenced by the shape of the suction side surface. The Mach number upstream of the profile and the inlet flow angle are not independent of each other. There is one particular incidence, the unique incidence [11], at which operation is possible.

Considering off-design operations, this shock system at the higher spans changes as the machine is throttled. At the choke point (lower back pressure and higher mass flow rate than design point, see Fig. 12, left), a double shock system occurs in the throat with a weak shock attached to the leading edge followed by a strong passage shock. At the design point (See Fig. 11), the oblique shock and the passage shock merge into a single shock. This is the optimal loss configuration. As the back pressure increases, the shock system moves ahead of the leading edge, eventually leading to stall (See Fig. 12, right).

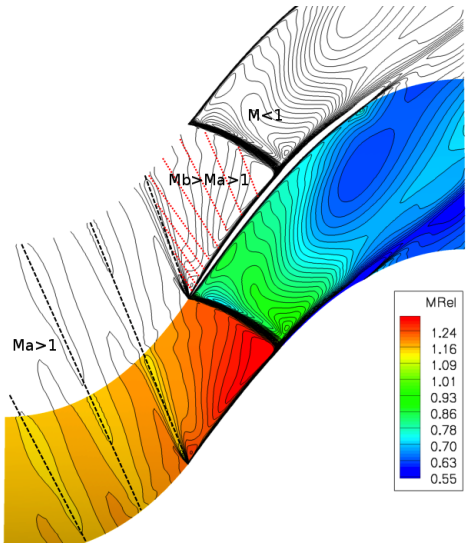

Figure 11: DENSITY FIELD AND MACH NUMBER LEVELS AT DESIGN POINT, 80% SPAN

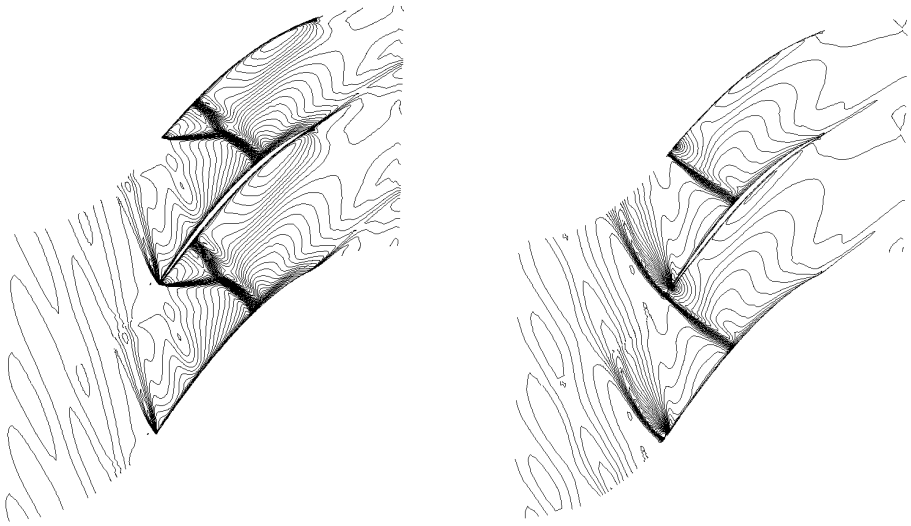

Figure 12: DENSITY FIELD AT CHOKE POINT (LEFT) AND NEAR STALL POINT (RIGHT), 80% SPAN

4.3. Aero-Mechanical Optimization

To guarantee the structural integrity of the fan rotor, a multi-disciplinary optimization is performed with the simultaneous evaluation of aerodynamic and mechanical performances. The blade geometry generated for the fluid evaluation is adapted to integrate a root that would be fastened to the disk, as well as a hub fillet radius. The solid geometry is then discretized using a finite element grid to enable the computation of the stresses.

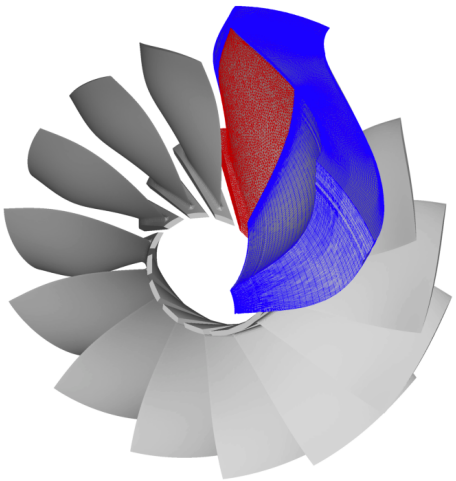

Figure 13: FLUID AND SOLID GRIDS

The solver Calculix [12] is used to compute the von Mises stresses in the blade. The following boundary conditions are applied:

- Centrifugal force
- Fixed translational degrees of freedom on the root faces
- Flow pressure load on both sides of the blade

Flow pressure values from the fluid solution are considered during the structure analysis, which follows the fluid computation for the performance evaluation of each design candidate. At each FEM node on both suction and pressure sides, the flow pressure value is interpolated from the fluid evaluation results with an inverse distance-weighted method. The interpolation is therefore influenced most by the nearby points and less by the more distant points. The FEM elements sharing a face on the blade sides are retrieved, and a pressure value is assigned to the face on the side, computed as the average of the values on its three corners. Figure 14 shows the pressure field on the suction side as a CFD result (left) and after interpolation on the FEM grid (right).

The von Mises stress evaluation reveals that the aero-optimal geometry exceeds the titanium yield strength limit by 109% (maximum stress of 1972 Mpa with a limit of 940Mpa). The stresses are distributed along the whole chord and span of the geometry (See Figure 15,left). Stress peaks are understood to originate from brutal camber change along the span. Figure 16 (left) illustrates a superposition of hub and tip section profiles projected on the circumferential plane. Even though very little contribution of lean and sweep is observed, severe spanwise evolution of the leading-

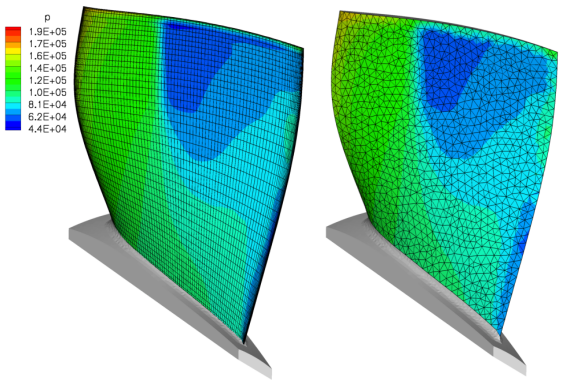

Figure 14: FLOW PRESSURE ON SUCTION SIDE OF CFD (LEFT) AND FEM (RIGHT) GRIDS

and trailing-edge position are shown with the curve linking the two profiles. The aero-mechanical optimal design exhibits a maximum stress of 639 Mpa, which represents a 65% reduction compared to the aerodynamic optimal design with only 1% loss in aerodynamic efficiency. The stress attenuation is understood as an effect of the smoother spanwise change of camber and a larger profile thickness at the hub.

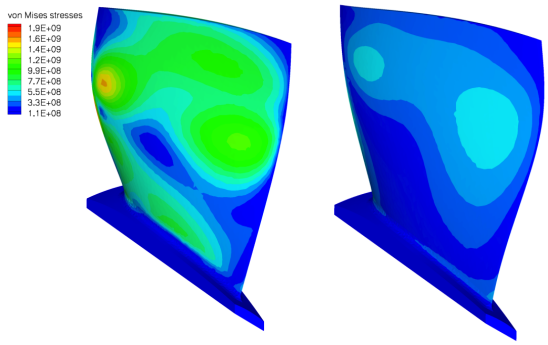

Figure 15: VON MISES STRESS ON SUCTION SIDE FOR AERO (LEFT) AND AERO-MECHANICAL (RIGHT) DESIGNS

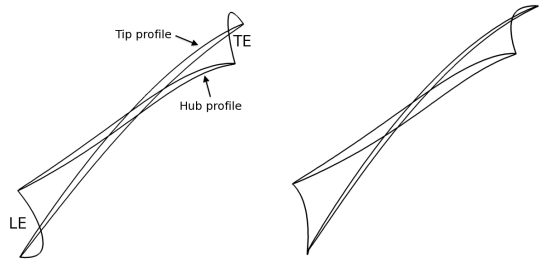

Figure 16: SECTION PROFILES STACKING FOR THE AERO (LEFT) AND AERO-MECHANICAL (RIGHT) DESIGNS

5. Conclusion

This paper presents the current status of the doctoral work entitled "Accelerated Optimization for Multi-Disciplinary Design of Transonic and Contra-Rotating Turbomachinery Components". The three main topics of investigation have been initiated and consists of: implementation of GPU-acceleration CFD, attenuation of shock interaction in transonic turbine, design and optimization of contra-rotating fan. The first part would result in the speed up aero-mechanical optimizations and will take place with progressive steps of implementation. In a second part, an optimized vane design for reduced downstream distortion has been achieved, providing a 43.2% reduction of downstream pitch-wise static pressure standard deviation. The unsteady interaction with the downstream rotor remains to be evaluated. In a third part, a methodology to design compact single-stage highly loaded axial flow fans has been proposed. Based on this, the simultaneous design of the two rotors of a contra-rotating fan is now targeted, considering both aerodynamic and mechanical performances.

References

[1] E. Elsen, P. LeGrelsey, E. Darve, "Large calculation of the flow over a hypersonic vehicle using a GPU", Journal of Computational Physics, 227(24), pp. 10148-10161, 2008

[2] T. Brandvik, G. Pullan, "An Accelerated 3D Navier-Stokes Solver for Flows in Turbomachines", ASME GT2009-60052, 2009

[3] NVIDIA, "NVIDIA CUDA Programming Guide", Version 3.1.1, 2010

[4] M.B. Giles, "Stator/Rotor Interaction in a Transonic Turbine", Journal of Propulsion, Vol.6, No.5, pp.621-627, 1990

[5] C. Sieverding, M. Stanislas, J. Snoeck, "The base pressure problem in transonic turbine cascades", Journal of Engineering for Power, Vol. 102, pp. 711718, 1980

[6] T. Verstraete, "CADO, a Computer Aided Design and Optimization Tool for Turbomachinery Applications", 2nd International Conference of Engineering Optimization, 2010

[7] A. Arnone, "Viscous Analysis of Three-Dimensional Rotor Flow Using a Multigrid Method", Journal of Turbomachinery, Vol. 116, pp. 435-445, 1994

[8] W. Calvert, R. Ginder, "Transonic Fan and Compressor Design", Journal of Mechanical Engineering Science, Vol. 213, N. 5, pp. 419-436, 1999

[9] S. Lieblein, F. Schwenk, F. Broderick, "Diffusion Factor for Estimating Losses and Limiting Blade Loadings in Axial Flow Compressor Blade Elements", NASA Research Memorandum AD011178, 1953

[10] G. Miller, G. Lewis, M. Hartmann, "Shock Losses in Transonic Rotor Rows", Journal of Engineering for Power, Vol. 83, pp. 235-242, 1961

[11] H. Lichtfuss, H. Starken, "Supersonic Cascade Flow", Progress in Aerospace Sciences, Vol. 15, pp. 37-149, 1974

[12] G. Dhondt, "The Finite Element Method for Three-Dimensional Thermomechanical Applications", Wiley, 2004